# Systemic Lymphoid Architecture Response Assessment (SYLARAS): An approach to multi-organ, discovery-based immunophenotyping implicates a role for CD45R/B220$^{+}$ CD8T cells in glioblastoma immunology

Gregory J. Baker[1,2,5*], Sucheendra K. Palaniappan[3], Jodene K. Moore[2], Stephanie H. Davis[1], Sandro Santagata[1,4,5,6,7] and Peter K. Sorger[1,2,5*]

[1]Laboratory of Systems Pharmacology, Program in Therapeutic Science, Harvard Medical School, Boston, MA 02115, USA.

[2]Department of Systems Biology, Harvard Medical School, Boston, MA 02115 USA.

[3]The Systems Biology Institute, Tokyo 141-0022 Japan.

[4]Department of Pathology, Brigham and Women's Hospital, Harvard Medical School, Boston, MA 02115 USA

[5]Ludwig Center for Cancer Research at Harvard, Harvard Medical School, Boston, MA

[6]Department of Oncologic Pathology, Dana Farber Cancer Institute, Boston, MA

[7]Department of Pathology, Boston Children's Hospital, Boston, MA

**Key Words:** SYLARAS (Systemic Lymphoid Architecture Response Assessment), systems immunology, glioblastoma (GBM)

**Running Title:** SYLARAS (Systemic Lymphoid Architecture Response Assessment)

**Corresponding Authors:**

Gregory J. Baker PharmD, PhD

American Cancer Society Postdoctoral Fellow

Tel: (617) 432-6909/ gregory_baker2@hms.harvard.edu

Peter K. Sorger PhD

Otto Krayer Professor of Systems Pharmacology

Tel: (617) 432-6901/ peter_sorger@hms.harvard.edu/ cc: christopher_bird@hms.harvard.edu

Laboratory of Systems Pharmacology

Department of Systems Biology

Harvard Medical School

200 Longwood Avenue

Warren Alpert Building, Room 440

Boston, MA 02115

**ABSTRACT**

Investigational and computational methods for the systematic exploration of global immune response are needed to gain a more integrated comprehension of disease and to explore the mechanisms of immunotherapy. Here were describe a modular and extensible framework for the acquisition, analysis, and visual display of systems-level immunophenotyping data called SYLARAS (Systemic Lymphoid Architecture Response Assessment, www.sylaras.org). Leveraging our technology against a syngeneic mouse model of glioblastoma (GBM) brain cancer, we reveal tumor-induced perturbation in the frequency and cell-to-cell co-variation of peripheral immune cell subsets hitherto undescribed in the disease. The most novel and significant of our findings relates to a population of $CD8^+$ T cells characterized by their expression of the CD45R/B220 isoform of the leukocyte common antigen, CD45 (aka $B220^+$ CD8T cells). In follow-on studies, we demonstrate that mouse $B220^+$ CD8T cells are a transcriptionally and morphologically-distinct subset of GBM-infiltrating lymphocytes whose human analog is identified in normal human blood and a subset of primary and recurrent GBM clinical biopsies. The ability of cells of this immunophenotype to attenuate immune response to autologous antigens, as demonstrated by the work of others, suggests that $B220^+$ CD8T cells may play an immunoregulatory role in GBM. By providing ample content for inductive scientific inference in the era of immunotherapy, SYLARAS has the potential to uncover complex cell and molecular mechanisms governing immunologic response.

## INTRODUCTION

Glioblastoma (GBM) is a rapidly progressing, incurable brain cancer that grows within the immunospecialized environment of the central nervous system. Like many other solid tumors, GBM exerts potent immunosuppressive effects on tumor-resident immune cells through its production of anti-inflammatory cytokines and catabolites[1,2,3,4,5,6,7], lectins[8,9], and immune checkpoint molecules[10,11,12]. Although the success of immunotherapy has been demonstrated to hinge on immunological events taking place outside of the tumor microenvironment (TME)[13,14,15], both the magnitude and biological significance of interactions occurring between peripheral and tumor-resident immune cell subsets is not well understood. This is in large part due to a lack of suitable tools for the systematic, longitudinal exploration of immune system composition, function, and network-level connectivity. In the specific case of GBM, the tumor's impact on the number, distribution, and activity of peripheral immune cells constituting the peripheral immune system is particularly unclear, as an in-depth multi-organ analysis of this tumor's impact on systemic immunity has not yet been performed.

Changes in immune cell number and allocation across lymphoid tissue as a result of the cellular migration, proliferation, and differentiation that accompanies the response to immunologic stimuli can is readily studied by immunophenotyping. The most common method for this is flow cytometry wherein combinations of antibody-based probes targeting integral membrane proteins, intracellular cytokines, and transcription factors are regularly and cost-efficiently used to characterize the frequency and function immune cell subsets. Evaluation of immunophenotypes from multiple lymphoid organs, among biological replicates, both in the presence and absence of an experimental immune perturbation (GBM in this work) poses a considerable analytical challenge[16]. Conventional tools that are well-suited to the analysis of a few samples, such as those with a native graphical user-interface (GUI) like FlowJo[17], become cumbersome and error-prone when applied to increasingly large datasets.

In this paper, we describe a set of software tools and experimental protocols that overcome the challenges of immunophenotyping across time and tissue that are collectively referred to as SYLARAS (Systemic Lymphoid Architecture Response Assessment). Application of its technology to the systematic identification and analysis of cellular immunophenotypes contained within a single-cell dataset spanning 240 tissue samples collected from 5 different lymphoid organs of age-matched mice inoculated with syngeneic mouse GBM cells or vehicle alone, reveals the breadth of impact intracranial tumor burden has on systemic immune cell populations. In making SYLARAS technology accessible to the greatest number of labs, we demonstrate the technique using standard 12-color flow cytometry; however, the approach is readily compatible with highly multiplexed methods such as mass cytometry (CyTOF)[18].

The key aspect of SYLARAS is its open-source computational analysis pipeline scripted in the Python programming language and useful for transforming single-cell data into a comprehensive overview of peripheral immune dynamics is response to immunologic disease and therapy. By providing parallel methods for knowledge-based and data-driven cell subset classification, SYLARAS allows for a direct comparison of the results obtained through supervised and unsupervised analysis. SYLARAS outputs a set of data-rich, easily interpretable graphical dashboards (1 per cell type) that serve as a concise compendium of the time and tissue-dependent changes occurring across multiple tissue sites in response to an arbitrary immune stimulus. We provide experimental protocols, source code, and details on flow cytometry antibodies and cytometer configuration settings, in addition to the full GBM immunophenotyping dataset, as open-access resources at www.sylaras.org.

In demonstrating the utility of the SYLARAS approach to discovery-based immunophenotyping, we follow-up on the most novel and statistically significant of our experimental findings which shows that CD45R/B220$^{+}$ CD8$^{+}$ T cells (aka B220$^{+}$ CD8T cells) behave differently in the presence of GBM

compared to conventional cytotoxic T cells. Through next-generation RNA-sequencing (RNA-seq), we show that B220$^{+}$ CD8T cells are transcriptionally-distinct from their B220- counterparts, while quantitative, spatially-resolved, single-cell analysis of 12-color immunofluorescence of the GBM TME reveals that the cells infiltrate the tumor mass where they are distinguishable in both spatial distribution and morphology from other tumor-infiltrating CD8$^{+}$ T lymphocytes. Complementary experiments in humans support a role for B220+ CD8T cells in GBM by showing that similar cells circulate in normal human blood and that a subset of primary and recurrent human GBM clinical biopsies. The ability of mouse and human B220$^{+}$ CD8T cells to attenuate immune response to autologous antigens[19,20], as demonstrated by the work of others, suggests B220$^{+}$ CD8T cells may have the potential to antagonize anti-tumor immune responses.

## RESULTS

### Multi-organ immunophenotyping of GBM-bearing mice by 12-color flow cytometry

We began our assessment of GBM's impact on peripheral immune system architecture by first titrating across a 250-fold dilution range 11 antibodies targeting various cell surface antigens expressed by a diverse array of immune cells to determine optimal immunolabeling concentrations (**Supplementary Fig. 1a**). Optical spillover among cytometry detection channels was tested and adjusted for through an optical control study (**Supplementary Fig. 1b**). As a further prelude to our longitudinal investigation, we next performed Kaplan-Meier survival analysis on a cohort of 10 C57BL/6J mice intracranially inoculated with $3x10^4$ syngeneic GL261 GBM cells to identify time points in tumor progression associated with early, middle, and late-stage disease (**Supplementary Fig. 1c**). After considering these results, and using a combination of our optimized and validated flow cytometry immunomarker panel and a methodical workflow (**Supplementary Fig. 1d-h**), we carried out 12-color flow cytometric analysis (11 immunomarkers plus fixable viability dye) on 5 lymphoid organs (blood, bone marrow, deep/superficial cervical lymph nodes, spleen, and thymus) from three age-matched cohorts of 8 GBM-bearing and 8 mock-engrafted mice at days 7, 14, and 30 post-tumor engraftment (N=48) (**Fig. 1**).

The overall the dataset consisted of 14 measurements (11 immunomarkers, cell viability, forward scatter (FSC) and side scatter (SSC)) made on each of $9.62x10^7$ immune cells spanning 240 tissue samples for a combined total of $1.25x10^9$ data points. Average cell viability across samples was 98.6% (range 90% - 99.7%) and differed between control and GBM-bearing animals only in the bone marrow at t=30-days where the percentage of dead cells was ~1.5-fold higher in control mice compared to those engrafted with GBM ($p = 0.005$, two-tailed Mann-Whitney U-test) (**Supplementary Fig. 1i**). Because the different lymphoid tissues varied in terms of their cell number (e.g. spleen >> blood), we elected to draw a $1x10^7$ cell weighted random sample (WRS) to equalize the number of cells analyzed per sample,

which yielded an average of $4x10^4$ cells per tissue sample (**Supplementary Fig. 1j**).

**A computer-assisted approach to systematic cell subset identification**

Immune cells are commonly identified based cell surface antigen expression which is scored as either present or absent (e.g. $CD_a^+$, $CD_b^-$, $CD_c^+$). To avoid the complexity, non-commutativity, and labor intensity inherent in serial gating in methodical evaluation of immunophenotypes present within our dataset, devised a strategy in which a distinction was made between true antibody signal and experimental noise on a per histogram basis using a computer-assisted procedure. In this unidimensional gating procedure, signal intensity histograms were displayed as a scrolling HTML table with kernel density estimates (KDEs) of unlabeled splenocytes super-imposed as fiducial guides aiding objective gate placement between background and foreground signal intensities. After a gate value for each of the dataset's 2,640 histograms (48 mice x 11 immunomarker channels x 5 tissues) had been recorded (a process which took less than 2 hours to complete) (**Fig. 2a-c** and **Supplementary Fig. 2**), the finalized table of gate values was fed back to the SYLARAS. From there SYLARAS zero-centered the signal intensity distributions associated with each histogram at the curated gate value by programmatically substance the gate value from all of the signal intensity measurements of their corresponding distributions. This caused signal intensities falling to the left of the gate, deemed as background autofluorescence, to become negative valued, which in turn allowed each cell in the dataset to be programmatically assigned an 11-dimensional Boolean vector fully specifying their immunophenotypes following a binarization procedure according to the mathematical sign (+/-) of performed on signal intensity values. For example, a cell associated assigned the Boolean vector [1, 0, 1, 1, 0, 0, 0, 1, 1 ,0, 0] would have fallen to the right-hand side of the gate for the A channel, the left-hand side of the gate for

the B channel, the right-hand side of the gate for the C, etc., and would have been associated with the corresponding immunophenotype: $CD_A^+ CD_B^- CD_C^+ CD_D^+ CD_E^- CD_F^- CD_G^- CD_H^+ CD_I^+ CD_J^- CD_K^-$. Although we settled on a computer-assisted supervised approach to cell subset identification, we had initially tested a series of fully-automated unsupervised methods for cell subset gating that included various Gaussian mixture models[21] and statistical thresholding methods[22], but found these and other methods to be insufficient for the task, as each were prone to gate misplacement.

**Characterization of mouse lymphoid tissue cellular architecture in 30 immunophenotypes**

Upon the completion of our cell subset identification procedure, we found that 604 of the 2,048 ($2^{11}$) possible Boolean immunophenotypes specified by our 11-immunomarker flow cytometry panel were represented by at least 1 cell. In limiting the scope of our downstream analysis, we elected to only consider those immunophenotypes whose frequency was $\geq$1% of cells in one or more of the study's 240 tissue samples. This dramatically reduced the number of immunophenotypes to just 30. Seeking to associate each of these high abundance immunophenotypes with an established immune cell type, we next developing a "dictionary" of cell surface antigen expression profiles that characterize landmark immune cell populations based on consensus literature. Fourteen (14) landmarks were defined: B, helper T (CD4T), myeloid dendritic (DC), cytotoxic T (CD8T), granulocyte (PMN), immature single-positive T (ISPT)[23], immature double-positive T (DPT), natural killer (NK), monocyte (Mono), macrophage (Mac), hematopoietic progenitor (Precursor), double-negative T (DNT), lymphoid tissue inducer (LTi)[24], and eosinophil (Eo) (**Fig. 3a**, inner wedges). To indicate the presence of specific variants of a given landmark population, we elected to prefix their aliases using conventional +/- immunophenotyping notation. For example, the subset of CD8T cells expressing Ly6C were assigned the alias $Ly6C^+$ CD8T

and were considered $CD8^+$ memory T cells[25,26] (**Fig. 3a**, outer wedges). Together, these 30 immunophenotypes accounted for 97% of the 10M cells comprising our WRS (**Fig. 3b**).

FSC and SSC light scatter measurements helped to benchmark the performance of our dictionary-based cell classification system by showing that the values of both parameters were lowest among cells classified as adaptive lymphocytes (e.g. $CD4^+$ and $CD8^+$ T cells); intermediate in innate lymphocytes and non-polymorphonuclear myeloid cells (e.g. NK cells, monocytes/macrophages, and dendritic cells); and highest among granulocytes (e.g. neutrophils/basophils) (**Fig. 3c**). The exceptionally high SSC of eosinophils allowed us to delineate these cells from macrophages, which in our study, shared the same antigen expression profile. Viewing our dataset from a tissue standpoint, the expected proportions of the different immunophenotypes were observed across the 5 lymphoid organs. For example, consistent with prior knowledge, the spleen, cervical lymph nodes, and blood were primarily composed of B cells and CD4 and CD8T cells, while much of the bone marrow was constituted by PMN cells,  B cells, and monocytes, and the thymus was near completely made up of ISPT and DPT immature thymocytes (**Fig. 3d**). Using information entropy (S) as a diversity metric, we next quantified heterogeneity in the distribution of the 30 immunophenotypes across the 5 lymphoid tissues tissues (**Fig. 3e**). This also agreed with known immunology, as ISPT and DPT cells were associated with the lowest entropy, due to their restriction to the thymus, while mature CD4 and CD8T cells were associated with relatively high information entropy scores, given that these cells are more evenly distributed throughout the immune system. Taken together, the results of our dictionary-based cell classification method were congruent with the known cellular architecture of the mouse immune system.

Given the existence of sophisticated algorithms for unsupervised cell subset identification, designed to meet the needs of highly multiplexed (30-40 channel) cytometry data and the extraordinary

insights into immune cell classification and functional state that they can provide[27,28,29,30,31], we sought to incorporate into SYLARAS the option for a data-driven perspective of the cell classes contained in a given dataset. In doing so, we elected to integrate a GUI-free implementation of the Phenograph[31] into our computational data analysis pipeline. To compare the results of our dictionary-based cell classification scheme with the unsupervised clustering results of Phenograph, it was necessary to further reduce the size of our 10M cell dataset subsample by a factor of 5 from ~42K cells per tissue sample to ~8K, as nearest-neighbor clustering algorithms like Phenograph tend to be computationally intensive[32]. We tested multiple integer values for the number of nearest neighbors (k, 10-30) using the standard Euclidean distance metric to determine the effect of this tunable parameter on cluster stability before settling on k=20 which returned a set of 30 clusters.

To quantify the fit of the 30 Phenograph clusters in terms of our dictionary-based cell classifier, we again turned to information entropy as a measure of diversity to evaluate heterogeneity in the dictionary-based immunophenotypes that made up each cluster (**Fig. 3f** and **Supplementary Fig. 3a**). Twenty (20) of the Phenograph clusters were in good agreement with prior knowledge, as a single immunophneotype accounted for ≥50% of their cell compositions. For example, 97% of the cells in cluster 1 mapped to the B cell immunophenotype. Conversely, the 10 remaining clusters were either conflicted (i.e. required more than one immunophenotype to account for ≥50% of their constituency) or were predominantly composed of cells unspecified by our immunophenotype dictionary (i.e. unclassified).

We noted that B cells were the consensus immunophenotype of clusters 1, 7, 9, 15, 16, and 18. While the brighter median CD45 and B220 signal intensity of cells constituting cluster 15 helped explain why they formed a distinct cluster, separation of the other 5 B cell clusters appeared to be due to differences in intrinsic background autofluorescence and/or off-target antibody binding

(**Supplementary Fig. 3b**). For example, the difference in CD11c, CD4, CD8α, and Ly6G signal intensity between the cells of cluster 1 and 7 was far greater than the difference in CD45 or B220 which are considered B markers. Although these differences may have *bona fide* biological underpinnings, separation of clusters based on apparent differences in background antibody binding could not be justified given the current experimental conditions. Nevertheless, the supervised and data-driven views of the same dataset offered by SYLARAS open the potential to generate novel hypotheses that might not have been formulated using one or the other method.

**SYLARAS reveals GBM-induced perturbation in the frequency of immune cell subsets hitherto undescribed in the disease**

To identify statistically significant differences in tissue-specific immune cell frequency between age-matched GBM-bearing and mock-engrafted mice, we next performed a set of 450 two-tailed Student's t-tests (30 cell classes x 5 tissues x 3 time points). After adjusting for multiple hypotheses by false discovery rate (FDR) correction, we identified 28 instances in which mean cell frequency diverged between tumor-burdened and control samples (q-value $\leq 0.05$) (**Fig. 4a**). Despite the majority of perturbations occurring during late-stage disease (t=30-day), increases in the frequency of DNT cells in the spleen and cervical lymph nodes of tumor-engrafted mice detected at the earliest time point (t=7-days). The increased frequency of the cells over control persisted in the spleen at the t=14-day time point and was consistent with the role played by DNT cells, including γ/δ T cells, in acute inflammatory immune response[33]. The increased frequency of CD8T cells observed in the bone marrow of late-stage GBM-bearing mice was also congruent with a recent report demonstrating the sequestration of T cells in the bone marrow of treatment-naïve humans and mice with GBM[34].

In terms of magnitude, the largest difference in immune cell frequency between control mice and those with tumor burden was a mean increase of 18% in circulating PMN cells (**Fig. 4b**). This observation was consistent with known facet of GBM immunobiology: namely, the accumulation of immature and immunosuppressive myeloid-derived suppressor cells (MDSCs) of the same immunophenotype (i.e. $CD45^+$ $CD11b^+$ $Ly6C^+$ $Ly6G^+$) in the blood of GBM-bearing mice and humans[35,36,37]. Additional differences of sizable magnitude included a reduction of 18% in circulating B cells and a 4% decrease in bone marrow-resident $Ly6C^-$ PMN cells, each occurring during the late-stage time point.

The fact that SYLARAS was capable of recapitulating known facets of GBM immunology bolstered our confident in interpreting perturbation in several other cell populations that were less expected. For example, we observed a wide-spread reduction in the abundance of hematopoietic progenitor cells (i.e. $CD45^+$ $lin^-$) throughout the bone marrow, cervical lymph nodes, and spleen of late-stage tumor-burdened mice. Although we are not the first to report on GBM's ability to influence bone marrow hematopoiesis, the ability of SYLARAS to uncover the breadth of the tumor's impact across multiple lymphoid organs is remarkable. Additional unexpected changes were reductions in splenic $CD3\varepsilon^-$ $CD4^+$ LTi cells thought to be important for lymphoid tissue organization, affinity maturation of germinal centers, and memory antibody responses[24] and increases in $Ly6C^+$ B cells in the cervical lymph nodes. Since the cervical lymph nodes a known sink for brain-derived antigens (PMID: 25100741) and Ly6C is a marker of antibody-producing plasma cells in mice[38], we postulated that the increase of these cells in response to late-stage tumor burden might have been indicative of an active, yet ineffectual, humoral immune response to the tumor. Also unexpected was a drop in the frequency of $F4/80^+$ B cells in the spleen of late-stage disease-bearing animals. Consistent with B cells bears macrophage-like characteristics called biphenotypic B/macrophages, the function of cells of this immunophenotype

remains enigmatic; however, the work of others suggests the requirements of macrophage colony-stimulating factor (M-CSF) and low levels of *Pax5* transcriptional activity for their development[39,40,41]. Before leaving the rest of the tumor-induced changes identified in peripheral immune cell frequency up to the reader's interest, we wish to point out that monotonic decreases in both splenic NK cells and circulating B220$^+$ CD8T cells changes were the two most statistically significant changes in the dataset with increasingly significant q-values across time points. Although NK cells have been previously implicated in GBM immunobiology[8,9,42], the tumor's effect on B220$^+$ CD8T cells appeared to be a novel. This previously documented subset of CD8$^+$ T cells expressing the CD45R/B220 isoform of the leukocyte common antigen, CD45[43]. Combining the statistics on fold-change and absolute abundance between test and control mice with the results of our exploratory analysis on cell class antigen expression, light scatter properties, and baseline tissue distribution, we programmatically generated a concise compendium of data-rich graphical dashboards (one per immunophenotype) that allowed complex, multi-organ immunophenotyping data on the tumor-induced changes in time and tissue-specific cell frequency to be portrayed in a readily interpretable format (**Fig. 4c** and **Supplementary Fig. 4**).

**Mouse-to-mouse variation in immunophenotype frequency holds network-level insight into GBM's immunomodulatory control over the peripheral immune system**

Despite our use of in-bred and age-matched animals, substantial between-subject biological variation (BSBV)[44] was observed between replicate control and tumor-burdened mice. The ability to identify biological outliers (aka exceptional responders) in complex immunologic response data can potentially increase our understanding of the individual and combinatorial features of immune response allied with disease progression and therapeutically favorable outcomes. Seeking to use mouse-to-mouse

variation to our advantage to test for biological outliers in our dataset and gain an overall perspective of variation in our dataset, we performed a principle component analysis (PCA). Together, PC1 and PC2 accounted for >60% of dataset variance; a good performance for PCA. The scores plot associated with these first 2 PCs revealed five primary clusters (**Fig. 5a**). The bone marrow and thymus samples (primary lymphoid tissues) were well-separated from the blood, spleen, cervical lymph nodes (secondary lymphoid tissues), and the blood and spleen exhibited substantial overlap. Variation was also evident within each cluster, being particularly apparent among blood and bone marrow samples.

Late-stage GBM-burdened mouse 3 was flagged as a significant outlier; its bone marrow, thymus, and blood samples were far removed from their respective primary clusters. Looking in further detail at the immunophenotypes contributing to mouse 3's outlier tendency, we identified higher fractions of mature myeloid cells, including DCs, macrophages, and Ly6C$^-$ PMN cells among its blood and bone marrow, and increased fractions of CD3ε$^+$ DPT cells (putative α/β-committed post-selection thymocytes[23]) and mature CD4$^+$ and CD8$^+$ T cell populations in its thymus that were suspicious of an ongoing immune response (**Fig. 5b**). Inspection of the SYLARAS dashboards revealed that the fraction of bone marrow Ly6C- PMN cells increased in control mice by 10-fold between the t=14 and t=30-day time point, a phenomemnon which failed to occur in tumor-burdened mice with the exception of mouse 3, whose fraction of cells was on par with that of controls (**Fig. 5c**). The increase in bone-marrow-resident Ly6C$^-$ PMN cells over time in control mice suggested that the cells may be a useful surrogate indicator of age-related changes in bone marrow composition; their failure to increase in GBM-bearing mice further suggests they may act as a cell-based biomarker of disease progression.

Although BSBV confounded our two-sample hypothesis tests by increasing dataset standard deviation and weakening p-values, we reasoned that it might contain additional information related to GBM's effect on peripheral immune system architecture. Using Spearman's rank-order correlation

(which requires replicate variation to be computed), we computed pairwise correlation between all time and tissue-specific immunophenotype pairs in control and GBM-burdened animals (e.g. splenic CD4T cells vs. thymic DPT cells in tumor-bearing mice at the t=30-day time point). In do so, we identified a set of 7 significant cell-to-cell correlations in control mice that were completely abrogated by the presence of GBM ($q \leq 0.05$) (**Fig. 5e**). The fact that the mean cell frequency of populations involved in significant correlations failed to reach statistical significance between control and tumor-burdened mice in our t-tests demonstrated that cell-to-cell covariation among biological replicates can arise independently of differences in population average value (**Fig. 5d**). many of the correlation pairs were readily explained by established immunology, such correlation #1, which can be explained based on the ability of monocyte/macrophages to induce B cell differentiation and survival[45], and correlation 5, which is in line with textbook interaction between MHC class II-expressing antigen-presenting cells and T helper cells. The potential biology underlying in some of the correlations was less apparent, however, we were interested to see correlation #2 involving $B220^{+}$ CD8T and B cells in the spleen, which served as an additional line of evidence suggesting GBM may influence these cells.

Given that correlation coefficients had been computed for all tissue-specific immunophenotype pairs in control and GBM-burdened mice, we next sought to infer GBM's impact on immunophenotypes involved in biologically-related processes by performing agglomerative hierarchical clustering on correlation profiles (vectors of correlation coefficients) of control and tumor-burdened mice (**Fig. 5f**). Silhouette analysis[46] was used to identifying the number of clusters (i.e. optimal linkage threshold) in each treatment group: 3 clusters were identified in control data, while 4 clusters where identified in data from GBM-burdened mice (**Fig. 5g,** (**Supplementary Fig. 5**). The most salient difference between mice of the two groups was the presence of cluster 3 in GBM-bearing mice. The cell populations constituting this cluster were strongly correlated, heavily enriched for DNT and PMN cells, and failed to co-cluster

in control mice. GBM cluster 3 was anti-correlated GBM clusters 1 and 2, which themselves were enriched for CD4T cells and various immune precursor cells. The observation of cluster 3 in mice with GBM burden is in accord with the results of a recent study in a spontaneous model of murine breast cancer wherein the authors provide compelling evidence for the ability of IL-17A-producing γδ T cells (consistent with the DNT immunophenotype in our study work given that >70% of γδ T cells are negative for both CD4 and CD8[47]) to induce an expansion of circulating neutrophils in tumor-bearing mice that are immunophenotypically matched with the PMN cells of our study[48]. We therefore postulate that co-variation between DNT cells and PMN cells in tumor-bearing hosts may reflect a more general phenomenon of cancer-induced immunomodulation discoverable through the purveyance of tools for systems-level immunophenotyping like SYLARAS.

**B220$^+$ CD8T cells are a transcriptionally-distinct subset of CD8$^+$ T lymphocytes differentially responsive to GBM-induced biological cues**

Based on the statistical significance and novelty of our SYLARAS-based findings up to this point related to B220$^+$ CD8T cells and the combined works of other groups who have attributed to these cells an ability to attenuate immune response to self-antigens both in mice and humans[19,20], we were compelled to continue investigating the nature of these cells and their relationship to GBM. Further analysis of our SYLARAS data showed that unlike CD4T cells, CD8T cells, in general, exhibit a broad and unimodal CD45R/B220 signal intensity distribution, with ~10% of cells in the blood, spleen, and cervical lymph nodes expressing the antigen at similar levels to B cells, which was defining of B220$^+$ CD8T cells (**Fig. 6a**). While the fraction of conventional CD8T cells in the thymus was ~4% across the study's 48 mice, the percentage of thymic B220$^+$ CD8T cells was in every mouse < 0.02% (**Fig. 6b**), suggesting that either B220 expression is induced after the cells have egressed from the thymus of that

they have extra-thymic developmental origins. The fact that the monotonic decrease in the frequency of circulating B220$^+$ CD8T cells in GBM-burdened mice was not mimicked by conventional CD8T cells (**Fig. 6c**) was further evidence that B220+ CD8T cells are distinct from other CD8$^+$ T cells. And finally, regression analysis revealed a strong positive relationship between the frequency of B220$^+$ and B220$^-$ CD8T cells in the spleen across multiple experimental conditions ($R^2$ = 0.6-0.9) that was selectively abrogated in mice bearing late-stage disease ($R^2$ = 0.004) (**Fig. 6d**), arguing for the differential-response of the CD8$^+$ T cell pool to the presence of GBM.

To directly test the hypothesis that B220$^+$ CD8T cells are indeed a biologically-distinct subset of CD8$^+$ T cells, we next performed RNA-seq on the coding transcriptome of B220$^{hi}$ and B220$^{lo}$ fractions of CD3ε$^+$ CD8α$^+$ T cells derived from the spleen of tumor-naïve C57BL/6J mice in biological replicate (n=2 B220$^{hi}$; n=3 B220$^{lo}$). Because B220$^+$ CD8T cells only account for ~1% of total splenocytes, if was necessary for us to combine the spleens of 5 mice prior to purifying these cells by fluorescence-activated cell sorting (FACS) (**Fig. 6e**). To expedite the sorting procedure, we B cells (~50-60% of splenocytes) were immunodepleted using anti-CD19 magnetic beads; the recovery of B220$^{hi}$ CD8T cells from CD19 immunodepleted spleens was itself evidence that B220$^+$ CD8T cells are indeed T cells, not B cells.

A PCA on the resulting transcript counts using the RNA-seq data analysis program, sleuth[49], revealed clear separation between B220$^{hi}$ and B220$^{lo}$ CD8T cell samples along PC1 (65% of dataset variation) (**Fig. 6f,g**). The contribution scores for PC1 showed that mRNA transcripts of mitochondrial genes most significantly impacted PC1's component scores, whereas a predicted gene (Gm26822) dominated as the most significant contributor to PC2's component scores (18% of dataset variation) and was, therefore, a likely of separation between the two B220$^{hi}$ CD8T cell samples (**Fig. 6h**). We were interested to also identify beta-2-microglobulin (*B2m*)—a component of the MHC class I complex—among the top 5 transcripts influencing PC2's component scores, which might reflect differences in the

ratio of classical MHC-class 1a and non-classical MHC-class 1b molecules present due to differences in sort purity between replicate samples .

To identify transcripts differentially expressed between the two populations, we subsequently performed a Wald test[50], which revealed 25 statistically significant (q-value $\leq$ 0.05) (**Fig. 6i**). The largest difference between B220$^{hi}$ and B220$^{lo}$ CD8T cells was a 7-fold reduction in B220$^{hi}$ cells in one of two splice variants encoding subunit 5 of the ARP2/3 complex (*Arpc5*, ENSMUST00000097536) involved in actin polymerization[51] and maintenance of T cell receptors (TCRs) at the cell surface[52] (beta-value = -7.0; q-value = $1.4 \times 10^{-7}$). Other differentially expressed transcripts with large fold-change and exceedingly low q-values encoded for Cullin 1 (*Cul1*), a component of the E3 ubiquitin ligase complex, and Diphthine methyl ester synthase (*Dph5*), a component of the diphthamide biosynthetic pathway which leads to the post-translational modification of histidine on elongation factor 2 (*Eef2*), which was interesting considering the fact that another translation elongation factor, 1α (*Eef1a*), provided the second largest contribution score to PC1. Taken together, the high contribution scores to PC1 given by transcripts associated with mitochondrial-encoded metabolic genes (*mt-Co1*, *mt-Atp6*, *mt-Cytb*, *mt-Nd4*), together with differentially expressed genes related to translation elongation (*Eef1a*, *Dph5*, and *Lars2*, *Rps9*) proteasome-mediated protein degradation (*Cul1*, *Ube2d3*, *Dtx2*), and glucose metabolism (*Gpi1*) suggested that the B220$^{hi}$ cells may be characterized by an altered metabolic state relative to conventional cytotoxic T cells.

**B220$^{+}$ CD8T cells are a morphologically and spatially distinguishable subset of GBM-infiltrating CD8$^{+}$ T lymphocytes**

To determine whether B220$^{+}$ CD8T infiltrate the GBM TME, we performed 12-color cyclic immunofluorescence imaging (CyCIF)[53,54] on tumor-bearing formalin-fixed paraffin-embedded (FFPE)

brain tissue sections using antibodies targeting many of the same cell surface antigens assayed by SYLARAS. Immunomarkers were first validated on mouse lymph node tissue sections (**Supplementary Fig. 7a,b** and **Supplementary Table 1**) prior to use on 5μm-thick mouse brain tissue sections bearing GL261 GBM at t=36-days. Scanning fluorescence imaging was performed using a 0.6 NA 40X objective to yield a mosaic image consisting of 168 400x300μm tiles from which quantitative, spatially-resolved, single-cell data on ~9 $x10^4$ cells was obtained following image segmentation (**Fig. 7a**). Using SYLARAS to analyze the data, we identified 7 abundant immunophenotypes in the tumor ipsilateral brain hemisphere among several other low abundance immunophenotypes (between 2 and 10 cells each) (**Fig. 7b** and **Supplementary Fig. 7c-f**). No immune infiltrate was observed in the contralateral hemisphere (data not shown).

Both $B220^+$ CD8T and conventional CD8T cells were present in the TME at approximately the same 1:10 ratio as that observed in the blood and spleen by SYLARAS. Compared to CD8T cells found in the TME, those expressing B220 tended to be more elongated and lacking in plasma membrane ruffling as observed in the CD8α channel (**Fig. 7c**). Tumor-infiltrating $B220^+$ CD8T cells also tended to exhibit stronger CD8α staining, which agreed with our data on circulating $B220^+$ CD8T cells whose median CD8α signal intensity was significantly higher than that of the conventional CD8T cell type ($p < 1x10^{-6}$) (**Fig. 7d**). The distribution of tumor-infiltrating $B220^+$ and $B220^-$ CD8T cells also differed. By comparing the density of the 7 abundant immune cell populations with that of the tumor (defined as $vimentin^+$ $lin^-$ cells), we found that conventional CD8T cells tended to localize to the tumor's margins, while the majority of the $B220^+$ CD8T cells were found at the center of the tumor mass (**Fig. 7e**). In quantifying the degree of overlap between these two immunophenotypes, we computed the spatial correlation of among all pairs of the 7 abundant immune cell types and the tumor itself (**Fig. 7f**). Correlation between $B220^+$ and $B220^-$ CD8T cells was far lower than what would have been expected if

the cells were drawn from the same underlying distribution ($R^2 = 0.26$). Based on the results of our multiplex immunofluorescence study, we conclude that $B220^+$ CD8T cells infiltrate the GBM TME where they look and behave differently from other tumor-infiltrating $CD8^+$ T lymphocytes.

Given that $B220^+$ CD8T cells were identified in the blood of tumor-naïve mice, we next sought to determine whether an analogous cell type could be found in normal human blood. In doing so, we surveyed ~$1.6x10^5$ peripheral blood mononuclear cells (PBMCs) obtained from a healthy human donor and fixed onto a glass microscope slide for immunolabeling with human-specific antibodies targeting CD3δ, CD8α and CD45R and scanning at 20x with a fluorescence microscope. Although anti-mouse CD45R/B220 antibodies (clone: RA3-6B2) are documented to cross react with human immune cells, we found that that these antibodies gave high background and lacked specific staining in the context of FFPE samples. Thus, as an alternative to the RA3-6B2 clone, we used anti-human CD45R (clone: MB1). These antibodies also recognize an epitope on exon-A of a high molecular weight isoform of CD45 expressed by human B cells and a subset of peripheral T cytotoxic/suppressor cells are validated on FFPE human tissue. Six (6) high-abundance immunophenotypes were observed (**Fig. 8a**). The bulk (~60%) of cells were negative for the 3 immunomarkers, which were followed in cell number by CD3δ single-positive cells, CD45R single-positive cells, CD3δ/CD8α double-positive T cells, and CD3δ/CD8α/CD45R triple-positive T cells (immunophenotypically analogous to mouse $B220^+$ CD8T cells) (**Fig. 8b**). Least abundant cell type was double-positive for CD3δ/CD45R which were thought to be enriched for $CD45R^+$ helper T cells[55].

To ultimately determine whether a $B220^+$ CD8T cell analogue could be identified in human GBM, we constructed and immunolabeled a tissue microarray (TMA) consisting of 312 FFPE 0.6mm in diameter core biopsies from 173 different brain tumor patients. The TMA contained 140 primary or recurrent grade-IV GBMs, 14 grade-II oligodendrogliomas, 14 grade-III anaplastic oligodendrogliomas,

2 grade-III anaplastic astrocytomas, and single cases of grade-III anaplastic astroblastoma, grade III anaplastic ganglioglioma, and FGFR3-TACC3 fusion glioma. Duplicate specimens from were present for the majority of patients, however, small differences in the level at which each core was paraffin embedded caused the failure of 16 cores to be transferred to the slide. Thus, a small subset of the patient's tumors we represented by just 1 core. The TMA was immunolabeled with the same antibodies used to probe human the blood and scanned at 20x using a fluorescence microscope to create a single mosaic image consisting of 875-tiles (**Fig. 8c**). Nineteen (19) of the 173 patients contained at least 1 CD3δ/CD8α/CD45R triple-positive cell; in one case, duplicate cores were both positive for these cells (patient #127) (**Fig. 8d-f**). Six (6) of the 19 tumors containing triple-positive cells were primary GBM, 10 were recurrent GBM, and the remaining 3 were a mixture of primary or recurrent anaplastic oligodendroglioma and astrocytoma, indicating that cells analogous to mouse $B220^+$ CD8T cells can be found in a variety of gliomas. Low numbers of triple-positive cells were attributed to small sample area, inhomogeneity in immune cell distribution across tissue, and the fact that the cells represent but a small fraction of total $CD8^+$ T cells (~10%). We conclude that $B220^+$ CD8T cells circulate in human blood and penetrate the TME of a subset of human GBM. Based on the work on others attributing immunosuppressive function to $B220^+$ CD8T both in mice and humans, we predict the cells to play an immunoregulatory role in the disease. In future studies, we aim to determine the diagnostic and/or immunotherapeutic potential of these cells in GBM and other cancers.

**DISCUSSION**

Given that immune outcomes depend on the coordinated activity of a network of specialized immune cells residing across multiple biological compartments[56], measures of individual aspects of the immune system are often poorly correlated with disease progression and therapeutic response. This fact underscores the value of studying model organisms that preserve in high-fidelity the biological context of complex immune repertoires through methods that integrate multi-tissue information at several biological scales. In achieving a more integrated comprehension of GBM's immunomodulatory influence, we have established an approach to multi-organ immunophenotyping of preclinical model systems called SYLARAS. The ultimately transforms quantitative single-cell data into a data-rich graphical compendium of the time and tissue-dependent changes occurring in lymphoid organ cellular constituency in response to an arbitrary immune stimulus. The systematic and concise format of presenting single-cell data through the SYLARAS dashboard facilities data interpretation and allows biological outliers to be easily identified while overcoming the inherent difficulty of representing large datasets using space-inefficient histograms and scatter plots. Supervised cell subset identification in SYLARAS is also streamlined, as an expedited unidimensional gating procedure leads to the rapid, yet systematic, identification of immune cell subsets preset within a dataset in a way that avoids the labor-intensity and non-commutativity inherent to serial gating. Integration of a GUI-free implementation of the nearest-neighbor clustering also allows for a unsupervised view of the cell subsets present in the same dataset.

Our work with SYLARAS in the context of a syngeneic mouse model of GBM has recapitulated known facets of GBM immunology while uncovering several others hitherto undescribed in the disease. The fact that CD45R/B220 expression by $CD8^+$ T cells does not create a bimodal distribution has likely contributed to the failure to identify a role for these cells in GBM and perhaps other cancers. The varied

works of others demonstrating the ability of immunophenotypically similar cells to attenuate immune response to autologous antigens suggests that the cells identified by our study may be capable of mitigating immune responses to potential tumor-derived neoantigens. Although true identity of B220$^+$ CD8T cells is unclear at present, at least two populations of T cells expressing CD45, CD3ε, CD8α, andCD45R/B220 have been previously characterized. One of which are known as CD8$^+$ T suppressor cells, which are capable of indirectly constraining immune response to self-antigens through interaction with specific subsets of CD4$^+$ T cells[57,58,59]. The other of which are intraepithelial lymphocytes (IELs) most commonly found in the gut mucosal lining[60]. Both cell types have also been documented to produce IL-10 and TGF-β—potent anti-inflammatory cytokines[59,60,61].

The *Ptprc* gene encodes an evolutionarily conserved phosphotyrosine phosphatase referred to as cluster of differentiation 45 (CD45). As an integral membrane protein expressed by all cells of the hematopoietic cell lineage, antibodies indiscriminately recognizing all isoforms of this alternatively spliced glycoprotein (referred to as anti-CD45) are useful probes in identifying immune cells as a class. However, antibodies whose binding to the protein is dependent on the presence of specific exons and carbohydrate moieties are referred to as anti-CD45R indicating their recognition of a “restricted” subset of splice variants. Antibodies such as this have been useful in delineating specific immune subsets[62,63]. For example, the anti-CD45R/B220 (clone: RA3-6B2) antibodies used in this study were initially included in the flow cytometry panel to label B cells despite their known immunoreactivity with subsets of NK cells[64] and T cells[65]. While the developmental regulation and biological significance of CD45R/B220 by CD8$^+$ T cells is incompletely understood, its expression is functional; its ligation with antibodies recognizing exon A of CD45R increase the proliferative response of T cells expressing the isoform to phytohemagglutinin (a mitogenic lectin)[43,66], which leaves open the possibility that CD45R/B220 may not just be a biomarker of these cells, but also play a direct role in mediating their

behavior in GBM. Whether the anti-CD45R/B220 (clone: RA3-6B2) and anti-CD45R (clone: MB1) used in this work in fact recognize an identical population of $CD8^+$ T cells in mice and man is uncertain. However, both antibodies are documented to react with restricted epitopes on exon A at the extracellular domain of a high molecular weight isoform of the CD45 glycoprotein expressed by human B cells and a subset of peripheral T cytotoxic/suppressor cells.

In conclusion, the potential of SYLARAS to provide ample content for inductive scientific inference of the cell and molecular mechanisms governing immunologically-relevant diseases as demonstrated through this work showcase its utility as a tool for immunologic discovery. Due to its modularity of design and its neutrality to the method of data acquisition, SYLARAS is compatible with various platforms for single-cell data acquisition, including flow cytometry (as demonstrated by the current work), CyTOF, and a series of rapidly emerging image-based technologies such as CyCIF[53,54], CODEX[67], and 4i[68] which offer the added benefit of providing insight into the spatial relationships among cells. Swapping the current set of 11 immunomarkers with different ones conjugated to the same (or similar) fluorophores will allow the investigator to follow-up on leads uncovered through initial immunophenotyping experiments with SYLARAS by focusing on cell surface and intracellular markers of specific immune lineages ensuring experimental continuity.

**METHODS**

Methods, including statements of data availability and any associated accession codes and references, are available in the online version of the paper.

Note: any Supplementary Information and Source Data files are available in the online version of the paper.

**ACKNOWLEDGMENTS**

This work was supported by an American Cancer Society Postdoctoral Fellowship (PF-16-197-01-LIB) to G.J.B, and by NIH/NCI grants P50-GM107618 and U54-CA225088 to P.K.S. We gratefully acknowledge Gabriel Berriz, Jeremy Muhlich, and Artem Sokolov for their support with computation.

**AUTHOR CONTRIBUTIONS**

G.J.B. conceived of the project; G.J.B and P.K.S developed the research; strategy G.J.B., S.H.D., and J.K.M. performed the experiments and analysis; G.J.B. and S.K.P. designed and performed the computational analysis; G.J.B. and P.K.S. wrote the paper.

## COMPETING FINANCIAL INTERESTS

The authors declare no competing financial interests.

**REFERENCES**

1. Maxwell, M., Galanopoulos, T., Neville-Golden, J. & Antoniades, H. N. Effect of the expression of transforming growth factor-beta 2 in primary human glioblastomas on immunosuppression and loss of immune surveillance. *J. Neurosurg.* **76**, 799–804 (1992).
2. Huettner, C., Czub, S., Kerkau, S., Roggendorf, W. & Tonn, J. C. Interleukin 10 is expressed in human gliomas in vivo and increases glioma cell proliferation and motility in vitro. *Anticancer Res.* **17**, 3217–3224 (1997).
3. Akasaki, Y. *et al.* Induction of a CD4+ T regulatory type 1 response by cyclooxygenase-2-overexpressing glioma. *J. Immunol.* **173**, 4352–4359 (2004).
4. Crane, C. A. *et al.* Immune evasion mediated by tumor-derived lactate dehydrogenase induction of NKG2D ligands on myeloid cells in glioblastoma patients. *Proc. Natl. Acad. Sci. U.S.A.* **111**, 12823–12828 (2014).
5. Wainwright, D. A. *et al.* IDO expression in brain tumors increases the recruitment of regulatory T cells and negatively impacts survival. *Clin. Cancer Res.* **18**, 6110–6121 (2012).
6. Zhou, W. *et al.* Periostin secreted by glioblastoma stem cells recruits M2 tumour-associated macrophages and promotes malignant growth. *Nat. Cell Biol.* **17**, 170–182 (2015).
7. Yan, J. *et al.* FGL2 as a Multimodality Regulator of Tumor-Mediated Immune Suppression and Therapeutic Target in Gliomas. *J. Natl. Cancer Inst.* **107**, (2015).
8. Baker, G. J. *et al.* Natural killer cells eradicate galectin-1-deficient glioma in the absence of adaptive immunity. *Cancer Res.* **74**, 5079–5090 (2014).
9. Baker, G. J., Chockley, P., Zamler, D., Castro, M. G. & Lowenstein, P. R. Natural killer cells require monocytic Gr-1(+)/CD11b(+) myeloid cells to eradicate orthotopically engrafted glioma cells. *Oncoimmunology* **5**, e1163461 (2016).

10. Wainwright, D. A. *et al.* Durable therapeutic efficacy utilizing combinatorial blockade against IDO, CTLA-4, and PD-L1 in mice with brain tumors. *Clin. Cancer Res.* **20**, 5290–5301 (2014).

11. Bloch, O. *et al.* Gliomas promote immunosuppression through induction of B7-H1 expression in tumor-associated macrophages. *Clin. Cancer Res.* **19**, 3165–3175 (2013).

12. Saas, P. *et al.* Fas ligand expression by astrocytoma in vivo: maintaining immune privilege in the brain? *J. Clin. Invest.* **99**, 1173–1178 (1997).

13. Spitzer, M. H. *et al.* Systemic Immunity Is Required for Effective Cancer Immunotherapy. *Cell* **168**, 487-502.e15 (2017).

14. Chen, D. S. & Mellman, I. Elements of cancer immunity and the cancer-immune set point. *Nature* **541**, 321–330 (2017).

15. Chen, D. S. & Mellman, I. Oncology meets immunology: the cancer-immunity cycle. *Immunity* **39**, 1–10 (2013).

16. Saeys, Y., Van Gassen, S. & Lambrecht, B. N. Computational flow cytometry: helping to make sense of high-dimensional immunology data. *Nat. Rev. Immunol.* **16**, 449–462 (2016).

17. FlowJo v10 Documentation. (2018).

18. Spitzer, M. H. & Nolan, G. P. Mass Cytometry: Single Cells, Many Features. *Cell* **165**, 780–791 (2016).

19. Takeuchi, T. *et al.* Functional characterization of the CD45R (2H4) molecule on CD8 (T8) cells in the autologous mixed lymphocyte reaction system. *Eur. J. Immunol.* **19**, 747–755 (1989).

20. James, E. A. & Kwok, W. W. CD8+ suppressor-mediated regulation of human CD4+ T cell responses to glutamic acid decarboxylase 65. *Eur. J. Immunol.* **37**, 78–86 (2007).

21. Melnykov, V & Maitra, R. Finite mixture models and model-based clustering. *Stat. Surv.* **4**, 80–116 (2010).

22. Otsu, N. A Threshold Selection Method from Gray-Level Histograms. *IEEE SMCS* **9**, 62–66 (1979).

23. Weerkamp, F., Pike-Overzet, K. & Staal, F. J. T. T-sing progenitors to commit. *Trends Immunol.* **27**, 125–131 (2006).

24. Lane, P. J. L., Gaspal, F. M. C. & Kim, M.-Y. Two sides of a cellular coin: CD4(+)CD3- cells regulate memory responses and lymph-node organization. *Nat. Rev. Immunol.* **5**, 655–660 (2005).

25. Walunas, T. L., Bruce, D. S., Dustin, L., Loh, D. Y. & Bluestone, J. A. Ly-6C is a marker of memory CD8+ T cells. *J. Immunol.* **155**, 1873–1883 (1995).

26. Hänninen, A., Maksimow, M., Alam, C., Morgan, D. J. & Jalkanen, S. Ly6C supports preferential homing of central memory CD8+ T cells into lymph nodes. *Eur. J. Immunol.* **41**, 634–644 (2011).

27. Spitzer, M. H. *et al.* IMMUNOLOGY. An interactive reference framework for modeling a dynamic immune system. *Science* **349**, 1259425 (2015).

28. Qiu, P. *et al.* Extracting a cellular hierarchy from high-dimensional cytometry data with SPADE. *Nat. Biotechnol.* **29**, 886–891 (2011).

29. Van Gassen, S. *et al.* FlowSOM: Using self-organizing maps for visualization and interpretation of cytometry data. *Cytometry A* **87**, 636–645 (2015).

30. Amir, E. D. *et al.* viSNE enables visualization of high dimensional single-cell data and reveals phenotypic heterogeneity of leukemia. *Nat. Biotechnol.* **31**, 545–552 (2013).

31. Levine, J. H. *et al.* Data-Driven Phenotypic Dissection of AML Reveals Progenitor-like Cells that Correlate with Prognosis. *Cell* **162**, 184–197 (2015).

32. Weber, L. M. & Robinson, M. D. Comparison of clustering methods for high-dimensional single-cell flow and mass cytometry data. *Cytometry A* **89**, 1084–1096 (2016).

33. D'Acquisto, F. & Crompton, T. CD3+CD4-CD8- (double negative) T cells: saviours or villains of the immune response? *Biochem. Pharmacol.* **82**, 333–340 (2011).

34. Chongsathidkiet, P. *et al.* Sequestration of T cells in bone marrow in the setting of glioblastoma and other intracranial tumors. *Nat. Med.* **24**, 1459–1468 (2018).

35. Kamran, N. *et al.* Immunosuppressive Myeloid Cells' Blockade in the Glioma Microenvironment Enhances the Efficacy of Immune-Stimulatory Gene Therapy. *Mol. Ther.* **25**, 232–248 (2017).

36. Gabrilovich, D. I. & Nagaraj, S. Myeloid-derived suppressor cells as regulators of the immune system. *Nat. Rev. Immunol.* **9**, 162–174 (2009).

37. Raychaudhuri, B. *et al.* Myeloid derived suppressor cell infiltration of murine and human gliomas is associated with reduction of tumor infiltrating lymphocytes. *J. Neurooncol.* **122**, 293–301 (2015).

38. Wrammert, J., Källberg, E., Agace, W. W. & Leanderson, T. Ly6C expression differentiates plasma cells from other B cell subsets in mice. *Eur. J. Immunol.* **32**, 97–103 (2002).

39. Graf, B. A. *et al.* Biphenotypic B/macrophage cells express COX-1 and up-regulate COX-2 expression and prostaglandin E(2) production in response to pro-inflammatory signals. *Eur. J. Immunol.* **29**, 3793–3803 (1999).

40. Borrello, M. A. & Phipps, R. P. Fibroblast-secreted macrophage colony-stimulating factor is responsible for generation of biphenotypic B/macrophage cells from a subset of mouse B lymphocytes. *J. Immunol.* **163**, 3605–3611 (1999).

41. Simmons, S. *et al.* Biphenotypic B-lymphoid/myeloid cells expressing low levels of Pax5: potential targets of BAL development. *Blood* **120**, 3688–3698 (2012).

42. Baker, G. J., Castro, M. G. & Lowenstein, P. R. Isolation and Flow Cytometric Analysis of Glioma-infiltrating Peripheral Blood Mononuclear Cells. *J Vis Exp* (2015). doi:10.3791/53676

43. Marvel, J. & Mayer, A. CD45R gives immunofluorescence and transduces signals on mouse T cells. *European Journal of Immunology* **18**, 825–828 (1988).

44. Sebastián-Gámbaro, M. A., Lirón-Hernández, F. J. & Fuentes-Arderiu, X. Intra- and inter-individual biological variability data bank. *Eur J Clin Chem Clin Biochem* **35**, 845–852 (1997).

45. Moore, P. A. *et al.* BLyS: member of the tumor necrosis factor family and B lymphocyte stimulator. *Science* **285**, 260–263 (1999).

46. Rousseeuw, PJ. Silhouettes: A graphical aid to the interpretation and validation of cluster analysis. *J. Comput. Appl. Math* **20**, 53–65 (1987).

47. Garcillán, B. *et al.* γδ T Lymphocytes in the Diagnosis of Human T Cell Receptor Immunodeficiencies. *Front Immunol* **6**, 20 (2015).

48. Coffelt, S. B. *et al.* IL-17-producing γδ T cells and neutrophils conspire to promote breast cancer metastasis. *Nature* **522**, 345–348 (2015).

49. Pimentel, H., Bray, N. L., Puente, S., Melsted, P. & Pachter, L. Differential analysis of RNA-seq incorporating quantification uncertainty. *Nat. Methods* **14**, 687–690 (2017).

50. Wald A. Sequential Tests of Statistical Hypotheses. *Ann. Math. Statist.* **16**, 117–186 (1945).

51. Welch, M. D., DePace, A. H., Verma, S., Iwamatsu, A. & Mitchison, T. J. The human Arp2/3 complex is composed of evolutionarily conserved subunits and is localized to cellular regions of dynamic actin filament assembly. *J. Cell Biol.* **138**, 375–384 (1997).

52. Zhang, Y. *et al.* Arp2/3 complex controls T cell homeostasis by maintaining surface TCR levels via regulating TCR+ endosome trafficking. *Sci Rep* **7**, 8952 (2017).

53. Lin, J.-R., Fallahi-Sichani, M. & Sorger, P. K. Highly multiplexed imaging of single cells using a high-throughput cyclic immunofluorescence method. *Nat Commun* **6**, 8390 (2015).

54. Lin, J.-R. *et al.* Highly multiplexed immunofluorescence imaging of human tissues and tumors using t-CyCIF and conventional optical microscopes. *Elife* **7**, (2018).

55. Bell, E. B. & Sparshott, S. M. Interconversion of CD45R subsets of CD4 T cells in vivo. *Nature* **348**, 163–166 (1990).

56. Rieckmann, J. C. *et al.* Social network architecture of human immune cells unveiled by quantitative proteomics. *Nat. Immunol.* **18**, 583–593 (2017).

57. Yu, Y. *et al.* Recent advances in CD8+ regulatory T cell research. *Oncol Lett* **15**, 8187–8194 (2018).

58. Filaci, G. & Suciu-Foca, N. CD8+ T suppressor cells are back to the game: are they players in autoimmunity? *Autoimmun Rev* **1**, 279–283 (2002).

59. Vukmanovic-Stejic, M., Thomas, M. J., Noble, A. & Kemeny, D. M. Specificity, restriction and effector mechanisms of immunoregulatory CD8 T cells. *Immunology* **102**, 115–122 (2001).

60. Cheroutre, H., Lambolez, F. & Mucida, D. The light and dark sides of intestinal intraepithelial lymphocytes. *Nat. Rev. Immunol.* **11**, 445–456 (2011).

61. Sun, M., He, C., Cong, Y. & Liu, Z. Regulatory immune cells in regulation of intestinal inflammatory response to microbiota. *Mucosal Immunol* **8**, 969–978 (2015).

62. Streuli, M., Hall, L. R., Saga, Y., Schlossman, S. F. & Saito, H. Differential usage of three exons generates at least five different mRNAs encoding human leukocyte common antigens. *J. Exp. Med.* **166**, 1548–1566 (1987).

63. Johnson, P., Greenbaum, L., Bottomly, K. & Trowbridge, I. S. Identification of the alternatively spliced exons of murine CD45 (T200) required for reactivity with B220 and other T200-restricted antibodies. *J. Exp. Med.* **169**, 1179–1184 (1989).

64. Blasius, A. L., Barchet, W., Cella, M. & Colonna, M. Development and function of murine B220+CD11c+NK1.1+ cells identify them as a subset of NK cells. *J. Exp. Med.* **204**, 2561–2568 (2007).

65. McNeill, L. *et al.* CD45 isoforms in T cell signalling and development. *Immunol. Lett.* **92**, 125–134 (2004).

66. Marvel, J., Poirier, G. & Lightstone, E. Anti-CD45RA antibodies increase the proliferation of mouse T cells to phytohemagglutinin through the interleukin 2/interleukin 2 receptor pathway. *Eur. J. Immunol.* **19**, 2005–2010 (1989).

67. Goltsev, Y. *et al.* Deep Profiling of Mouse Splenic Architecture with CODEX Multiplexed Imaging. *Cell* **174**, 968-981.e15 (2018).

68. Gut, G., Herrmann, M. D. & Pelkmans, L. Multiplexed protein maps link subcellular organization to cellular states. *Science* **361**, (2018).

69. Telford, W. G., Babin, S. A., Khorev, S. V. & Rowe, S. H. Green fiber lasers: an alternative to traditional DPSS green lasers for flow cytometry. *Cytometry A* **75**, 1031–1039 (2009).

70. Parks, D. R., Roederer, M. & Moore, W. A. A new 'Logicle' display method avoids deceptive effects of logarithmic scaling for low signals and compensated data. *Cytometry A* **69**, 541–551 (2006).

71. McDonald, B., Urrutia, R., Yipp, B. G., Jenne, C. N. & Kubes, P. Intravascular neutrophil extracellular traps capture bacteria from the bloodstream during sepsis. *Cell Host Microbe* **12**, 324–333 (2012).

72. Barnard, M. R. *et al.* Effects of platelet binding on whole blood flow cytometry assays of monocyte and neutrophil procoagulant activity. *J. Thromb. Haemost.* **3**, 2563–2570 (2005).

## ONLINE METHODS

*General reagents*

$ddH_20$; RPMI-1640 (Corning, Cat. No. 10-040-CV); L-glutamine (Gibco, Cat. No. 25030-081); penicillin-streptomycin (10,000 U/mL) (ThermoFisher Scientific, Cat. No. 15140-163); heat-inactivated (HI) fetal bovine serum (FBS) (Gibco, Cat. No. 16140-071); Dulbecco's phosphate buffered saline (DPBS) w/o $CaCl_2$, $MgCl_2$ (Corning, Cat. No. 21-040-CV); 5% (w/v) sodium azide ($NaN_3$) (BDH, Cat. No. BDH7465-2); ethylenediaminetetraacetic acid (EDTA) disodium salt dehydrate ($C_{10}H_{14}N_2Na_2O_8 \bullet 2H_2O$) (Sigma Aldrich, Cat. No. ED2SS); 15 mL polypropylene conical tubes (Falcon, Cat. No. 352097); 50 mL polypropylene conical tubes (Falcon, Cat. No. 352098); 5 mL polystyrene serological pipettes (Corning, Cat. No. 4050); 10 mL polystyrene serological pipettes (Corning, Cat. No. 4100); micropipettes (1000 µL, 200 µL, 20 µL, 10 µL) (Gilson); research plus 12-channel pipette (50-300 µl), (Eppendorf, Cat. No. 3122000060); 0.1-10 µl TipOne natural pipet tips (USA Scientific, Cat. No. 1111-3200); 1.0-20 µl TipOne natural pipet tips (USA Scientific, Cat. No. 1120-1810); 1-200 µl TipOne natural pipet tips (USA Scientific, Cat. No. 1111-1200); 101-1,000 µl TipOne natural pipet tips (USA Scientific, Cat. No. 1111-2820); 40 µm nylon mesh cell strainers (Falcon, Cat. No. 352340); 2 L polyethylene Dewar flask (Nalgene, Cat. No. 4150-2000); sterile cryogenic storage vials (Sigma-Aldrich, Cat. No. V7634); mini vortexer 120V (VWR, Cat. No. 58816-121); polypropylene general-purpose test tube racks (Nalgene, Cat. No. 5930-0020); 96-well reversible microcentrifuge tube rack (Bio Plas, Cat. No. 0091); S1 pipet filler (ThermoFisher Scientific, Cat. No. 9531); 9 L TruCool rectangular ethylene-vinyl acetate foam ice pans (BioCision, Cat. No. BCS-112); 1.5 mL microcentrifuge tubes (USA Scientific, Cat. No. 1615-5500); gel loading tips (Costar, Cat. No. 4853); 60 mm x 15 mm polystyrene tissue culture dishes (Falcon, Cat. No. 353002); 0.4% trypan blue solution (Gibco, Cat. No. 15250061)

*Reagents germane to mouse euthanasia, perfusion, and tissue processing*

ketamine hydrochloride injection (VEDCO, NDC: 50989-996-06); xylazine hydrochloride injection (AKORN INC, NDC: 59399-111-50); 0.9% sodium chloride (NaCl) injection, USP (Hospira, NDC 0409-4888-10); 1 mL Norm-Ject® sterile Luer-slip syringes (Henke Sass Wolf, Cat. No. 4010.200V0); PrecisionGlide needles - 26G x ½ (0.45 mm x 13 mm) (BD, Cat. No. 305111); sodium chloride (NaCl) (Sigma Aldrich, Cat. No. S9888); calcium chloride ($CaCl_2$•$2H_2O$) (Sigma Aldrich, Cat. No. C8106); sodium phosphate monobasic ($NaH_2PO_4$•$2H_2O$) (Sigma Aldrich, Cat. No. 71505); D-glucose ($C_6H_{12}O_6$) (Sigma Aldrich, Cat. No. G8270); sodium bicarbonate ($NaHCO_3$) (Sigma Aldrich, Cat. No. S5761); potassium chloride (KCl) (Sigma Aldrich, Cat. No. P9333); heparin sodium salt from porcine intestinal mucosa (Sigma-Aldrich, Cat. No. H4784); extruded polystyrene foam block (2); Halsted-mosquito hemostat (2) (Fine Science Tools, Cat. No. 13008-12); fine scissors—martensitic stainless steel (2) (Fine Science Tools, Cat. No. 14094-11); Friedman rongeur (Fine Science Tools, Cat. No. 16000-14); Littauer bone cutters (Fine Science Tools, Cat. No. 16152-12); cover-glass forceps (Fine Science Tools, Cat. No. 11073-10); Dumont #5 forceps (2) (Fine Science Tools, Cat. No. 11252-40); Graefe forceps (2) (Fine Science Tools, Cat. No. 11051-10); Masterflex L/S digital pump system with easy-load II pump head, 600 RPM, 115/230V (Cole-Parmer, Cat. No. EW-77921-75); 20 G x 1 1⁄2" aluminum hub blunt needles (Kendall, Cat. No. 8881202363); razor blades (VWR, Cat. No. 55411-050); frosted microscope slides (Fisher Scientific, Cat. No. 12-550-343); 3 mL Luer-Lok® syringes (BD, Cat. No. 309657); PrecisionGlide needles - 23G x 1 (0.6 mm x 25 mm) (BD, Cat. No. 305145); Falcon 3 mL polyethylene transfer pipets (Corning, Cat. No. 357524)

*Reagents germane to immunolabeling*

Brilliant Stain Buffer (BD Biosciences, Cat. No. 563794); TruStain FcX anti-mouse CD16/32 antibody (BioLegend, Cat. No. 101320); fixable viability dye, eFluor 455UV (eBioscience, Cat. No. 65-0868-14); Brilliant Ultraviolet 737-conjugated anti-mouse CD11b, clone: M1/70, isotype: rat DA/HA IgG2b, κ (BD Biosciences, Cat. No. 564443); V500-conjugated anti-mouse CD45, clone: 30-F11, isotype: rat LOU/M IgG2b, κ (BD Biosciences, Cat. No. 561487); Brilliant Violet 605-conjugated anti-mouse CD4, clone: RM4-5, isotype: rat IgG2a, κ (BioLegend, Cat. No. 100548); Brilliant Violet 711-conjugated anti-mouse Ly6G, clone: 1A8, isotype: rat IgG2a, κ (BioLegend, Cat. No. 127643); Alexa Fluor 488-conjugated anti-mouse CD3ε, clone: 145-2C11, isotype: Armenian hamster IgG (eBioscience, Cat. No. 53-0031-82); PE/Cy7-conjugated anti-mouse CD49b, clone: HMα2, isotype: Armenian hamster IgG (BioLegend, Cat. No. 103518); PE-conjugated anti-mouse F4/80, clone: BM8, isotype: rat IgG2a, κ (BioLegend, Cat. No. 123110); PE-CF594-conjugated anti-mouse CD8α, clone: 53-6.7, isotype: rat LOU/M IgG2a, κ (BD Biosciences, Cat. No. 562283); PerCP/Cy5.5-conjugated anti-mouse/human CD45R/B220, clone: RA3-6B2, isotype: rat IgG2a, κ (BioLegend, Cat. No. 103236); Alexa Fluor 647-conjugated anti-mouse CD11c, clone: N418, isotype: Armenian hamster IgG (BioLegend, Cat. No. 117312); APC/Cy7-conjugated anti-mouse Ly6C, clone: HK1.4, isotype: rat IgG2c, κ (BioLegend, Cat. No. 128026); V500-conjugated rat IgG2b, κ isotype control antibody, clone: A95-1, isotype: rat LOU/M IgG2b, κ (BD Biosciences, Cat. No. 560784); purified anti-human CD45R, clone: MB1, isotype: mouse IgG1 (Abnova, Cat. No. MAB16165); Alexa Fluor 488-conjugated anti-human CD8α, clone: AMC908, isotype: mouse IgG2a, κ (eBioscience, Cat. No. 53-0008-80); Alexa Fluor 555-conjugated anti-human CD3δ, clone: EP4426, isotype: rabbit IgG (abcam, Cat. No. AB208514); fixation/permeabilization solution kit (BD Biosciences, Cat. No. 554714); 4',6-diamidino-2-phenylindole, dihydrochloride (DAPI) (ThermoFisher Scientific, Cat. No. D1306); 96-well V-bottom, non-treated, polystyrene microplate

(Costar, Cat No. 3897); 12-well V-bottom reagent reservoir (Argos Technologies, Cat. No. B3135); Microseal 'F' foil seal (Bio-Rad; Cat. No. MSF1001)

*Reagents germane to flow cytometry*

Sphero rainbow fluorescent particles (3.0-3.4 μm) (BD Biosciences, Cat. No. 556291); FACSDiva CS&T research beads (BD Biosciences, Cat. No. 655051)

**Mice**

Twelve-week-old female C57BL/6J mice syngeneic to the mouse GL261 GBM model were used in this study (Jackson Laboratory, Bar Harbor, ME). All animal experiments were conducted in accordance with procedures preapproved by the Institutional Animal Care and Use Committee (IACUC) and conformed to the policies and procedures of the Center for Comparative Medicine at Harvard Medical School in agreement with the National Research Council's "Guide for the Care and Use of Laboratory Animals".

**Cell Line**

The GL261 GBM cell line was obtained from the Developmental Therapeutics Program (DTP), Division of Cancer Treatment and Diagnosis (DCTD) tumor repository through a material transfer agreement with the Biological Testing Branch (BTB) of the National Cancer Institute (NCI).

**Clinical Specimens**

All deidentified human brain tumor resections used in this study were obtained from consented patients under care at Brigham and Women's Hospital or Dana-Farber Cancer Institute in association with Institutional Review Board (IRB) protocols: 10-417 or 11-104 (17-000).

**Major Equipment**

BD LSR II Special Order Research Product (SORP) flow cytometer w/ BD High Throughput Sampler (HTS):

- Laser line – power:
    - 488 nm laser – 20 mw (run at 20 mw)
    - 405 nm laser – 50 mw (run at 50 mw)
    - 594 nm laser – 200 mw (run at 125 mw)
    - 355 nm laser – 20 mw (run at 20 mw)

BioTek EL406 automated microplate washer/dispenser:

- In an effort to minimize cell loss, aspiration steps involving 96-well V-bottom microplates were performed using this instrument such that a 50 µL residual volume remained after each aspiration. This factor was accounted for in all reported dilutions. Instrument configurations were as follows:
    - plate type: 96-well
    - W-aspirate
    - vacuum filtration: false
    - travel rate: 1 (4.1 & 1.0 mm/sec)
    - delay: 0 msec
    - z-offset: 55 steps (6.99 mm above carrier)

  - x-offset: 0 steps (center of well)
  - y-offset: 0 steps (center of well)
  - secondary aspirate: no

Beckman Coulter Avanti J-26XP centrifuge:

- JS-5.3 anodized aluminum swinging-bucket rotor (Beckman Coulter, Cat. No. 368690)

Bransonic CPXH ultrasonic cleaning bath:

- model 3800

**Reagent Preparation**

supplemented RPMI-1640 (RPMI-1640 with L-glutamine, 100 U/mL penicillin-100 U/mL streptomycin, 10% HI-FBS, 0.05% sodium azide):

- to a 500 mL bottle of RPMI-1640 with L-glutamine were added:
  - 5 mL of a 10,000 U/mL penicillin-10,000 µg/mL streptomycin solution
  - 50 mL of HI-FBS
  - 2.5 mL of a 5% w/v sodium azide solution
  - 5 mL of a 10% EDTA solution

heparinized Tyrode's solution:

- to a 1 L glass screw-cap storage bottle on a stirring plate and containing a magnetic stirring bar and 1 L dd$H_2O$ were added:
  - 8.0 g sodium chloride
  - 0.264 g calcium chloride
  - 0.05 g sodium phosphate monobasic

  - 1.0 g D-glucose
  - 1.0 g sodium bicarbonate
  - 0.2 g potassium chloride
  - 100 U of heparin sodium
- Salts were allowed to completely dissolve prior to storage at 4 °C.

ammonium-chloride-potassium (ACK) lysis buffer (1X):

- to 1 L of stirring $ddH_20$ were added:
  - 8.29 g of ammonium chloride
  - 1.0 g of potassium bicarbonate
  - 37.2 mg of sodium EDTA
- pH was adjusted to 7.4

flow buffer (DPBS + 0.5% HI-FBS):

- to 95 mL of DPBS was added:
  - 0.5 mL of HI-FBS
- stored at 4°C

flow buffer + azide (flow buffer + 0.05% sodium azide):

- to 49.5 mL of flow buffer was added:
  - 0.5 mL of a 5% w/v sodium azide solution
- stored at 4°C

EDTA solution (1X DPBS containing 10% EDTA):

- to 50 mL of DPBS was added:
  - 5 g of disodium EDTA

- placed in ultrasonic bath to facilitate dissolution
- stored at 4°C

Fc block (flow buffer + azide containing 22.5 µg/mL anti-mouse CD16/32):

- refer to accompanying spreadsheet for preparation details (**Supplementary Table 2**).

fixable viability dye:

- eFluor 455UV fixable viability dye was diluted 1.5:1,000 in 1X DPBS
- refer to accompanying spreadsheet for preparation details (**Supplementary Table 2**).

**Antibody Titration**

Immunolabeling concentrations yielding the highest staining index (SI)[69] for each antibody in the study were determined by first harvesting the spleens of two 12-week-old female C57BL/6J mice placed under terminal anesthesia with a dose of 150 mg/kg of ketamine hydrochloride and 20 mg/kg xylazine hydrochloride diluted in sterile 0.9% NaCl delivered with a 1 mL tuberculin syringe equipped with a 26G needle as a single intraperitoneal (i.p.) injection. Using opposing frosted ends of 2 glass microscope slides, each spleen was gently macerated and rinsed with 4 mL of supplemented RPMI-1640 into a 60 x 15 mm polystyrene petri dish on ice. Splenocytes were aspirated from the dish, dispensed into a 15 mL conical tube, and centrifuged at 350 x g (max RCF) for 10 minutes at 4°C. The cell pellet was resuspended in 8 mL of a 1X ACK lysing buffer and placed on ice for 5 minutes to lyse red blood cells (RBCs). Six (6) mL of flow buffer + azide was added to the tube prior to filtering the cell suspension through a 40 µm nylon mesh into a fresh 15 mL conical tube. Splenocytes were again centrifuged at 350 x g (max RCF) for 10 minutes at 4°C then resuspended in 2 mL of flow buffer + azide. Cell counting

was performed using a trypan blue and a glass hemocytometer. Cell concentration was adjusted accordingly to achieve a final concentration of $1x10^7$ cells/mL.

Two-hundred (200) µL of the $1x10^7$ cell/mL splenocyte suspension were added to wells A-H of 11 concentric columns of a 96-well V-bottom microplate using a multichannel pipette followed by centrifugstion at 100 x g (max RCF) for 3 minutes at 4°C. One-hundred and fifty (150) µL of cell supernatant was aspirated from each well followed by resuspension in 100 µL of Fc block (15 µg/mL final concentration). Splenocytes were incubated on ice for 5 minutes prior to centrifugation at 100 x g (max RCF) for 3 minutes at 4°C. One-hundred (100) µL was aspirated from each well before resuspension with 100 µL of target antibodies pre-diluted in Brilliant Stain Buffer to achieve the following two-fold serial dilution series per column for each of the 11 antibodies used in the study: 24, 12, 6, 3, 1.5, 0.75, 0.375, and 0.1875 µg/mL. Splenocytes were immunolabeled on ice for 15 minutes in the dark prior to centrifugation at 100 x g (max RCF) for 3 minutes at 4°C. Two-hundred (200) µL of supernatant were then aspirated followed by resuspension with 100 µL of flow buffer + azide. This washing step was repeated once except that 200 µL (instead of 100 µL) of flow buffer + azide was used in the resuspension step. DAPI was added to each well at a final concentration of 1µg/mL and allowed to incubate for 3-5 minutes prior to data acquisition.

Immunolabeled splenocytes were analyzed on a BD LSR II SORP flow cytometer equipped with a BD HTS for 96-well high-throughput sampling. The following acquisition gating strategy was used: (FSC-A vs. SSC-A) → (SSC-H vs. SSC-W) → (FSC-H vs. FSC-W) → (DAPI-A vs. FSC-A) → ($CD_x$ vs. count). A total of 10,000 viable singlets were analyzed per well. The median fluorescence intensities (MFIs) of the first (background) and second (first true positive) peaks, and the $84^{th}$ percentile of the first peak were identified using the layout editor tool of FlowJo software from which a SI for each antibody was calculated according to the following formula: $SI = (MFI_{pos}-MFI_{neg})/[(84\%_{neg}-MFI_{neg})/0.995]$. The

maximum SI ($SI_{max}$) of each antibody was used as the target immunolabeling concentration in our longitudinal study.

**Stereotactic Engraftment of GBM Cells into the Mouse Brain**

The reader is referred here[42] for detailed instruction on how to stereotactically engraft glioma cells into the mouse brain.

**Tissue Harvesting and Processing**

The following disposable reagents were gathered and labeled before each of our study's 3 time points:

- 15 mL conical tubes (16)
    - labeled: "blood", <condition>, <replicate> (note: < > indicates a variable)
- 3 mL syringes equipped with 23G needles (16)
    - labeled: "marrow", <condition>, <replicate>
- 1 mL tuberculin syringes equipped with 26G needles (17)
    - (16) labeled: "blood", <condition>, <replicate>
    - (1) unlabeled: used for injectable anesthesia
- 60 x 15 mm polystyrene petri dishes (64)
    - labeled: <tissue> (excluding blood), <condition>, <replicate>
    - 4 mL of supplemented RPMI-1640 was added to each dish
- 0.5 mL microcentrifuge tubes (80)
    - labeled: <tissue>, <condition>, <replicate>

One-hundred (100) µL of a 10% EDTA solution was added to each 15 mL conical tube. Four (4) mL of supplemented RPMI-1640 was added to each 60 x 15 mm polystyrene petri dish with the exception of

those labeled "marrow", to which only 2 mL of supplemented media was added (the other 2 mL of supplemented RPMI-1640 was to be placed into each of the (16) 3 mL syringes). One-hundred ninety-eight (198) µL of flow buffer was added to each microcentrifuge tube. Fifty (50) µL of a 10% EDTA solution was added to each 1 mL tuberculin syringe to coat the inner barrel with EDTA by operating the plunger several times. All conical tubes, petri dishes, 3 mL syringes, and microcentrifuge tubes were stored on ice or at 4°C.

Sixteen (16) mice were terminally anesthetized in series with a 150 mg/kg of ketamine hydrochloride and 20 mg/kg xylazine hydrochloride diluted in sterile 0.9% NaCl delivered with the unlabeled 1 mL tuberculin syringe as a single i.p. injection. Refer to accompanying spreadsheet for preparation details (**Supplementary Table 2**). Once non-responsive to both toe and tail pinch, each mouse was pinned ventral side up to an extruded polystyrene foam block by its front and hind paws using four 26G needles and sprayed down with 70% EtOH to prevent fur from entering the dissection cavity. Lymphoid organs were harvested in the following order: blood, thymus, spleen, superficial/deep cervical lymph nodes, bone marrow. *Blood*: after making a "y" incision from the gut to the rib cage to expose the heart, whole blood was aspirated from the right ventricle directly into one of the aforementioned EDTA-coated 1 mL tuberculin syringes. The needle was removed before expelling blood into its respectively labeled 15 mL conical tube stored on ice. Each mouse was then transcardially perfused with heparinized and oxygenated (95% $O_2$/5% $CO_2$) Tyrode's solution at a rate of 4.0 mL/minute for at least 2 minutes in a laminar flow hood to fully exsanguinate the circulatory system. The method for mouse transcardial perfusion has been described in detail elsewhere[42]. *Thymus*: Once exsanguinated, each mouse was returned to the extruded polystyrene foam block for thymus excision with small dissection scissors and fine-tipped bent forceps being careful to remove any contaminating adipose and the mediastinal lymph nodes. Thymi were placed into respectively labeled 60 x 15 mm

polystyrene petri dishes on ice. *Spleen*: Spleens were excised using small dissection scissors and fine-tipped bent forceps and placed into respectively labeled 60 x 15 mm polystyrene petri dishes on ice. *Superficial/deep cervical lymph nodes*: Lymph nodes were dissected under a dissection microscope using small dissection scissors and fine-tipped bent forceps. Excised nodes were placed into respectively labeled 60 x 15 mm polystyrene petri dishes on ice. *Bone marrow*: The right hind limb of each mouse was removed using bone cutters. Musculature and tendons were stripped away from the femur and tibia and the proximal and distal epiphyses of each bone were removed using a single-edged razor blade. Marrow from the two bones was flushed into the respectively labeled 60 x 15 mm polystyrene petri dish on ice using the 2 mL of supplemented RPMI-1640 in the respectively labeled 3 mL syringe. Flushed marrow was gently aspirated and expelled back into the petri dish one time to facilitate cell dissociation.

Thymi, spleens, and cervical lymph nodes were macerated using opposing frosted ends of 2 glass microscope slides which were dipped into the 4 mL of supplemented RPMI-1640 of the respectively labeled 60 x 15 mm polystyrene petri dish to collect as may cells as possible. Plastic Pasteur pipettes were used to transfer lymph nodes onto the frosted end of one glass microscope slide for maceration. A fresh pair of slides were used for each tissue to prevent sample cross-contamination. Five (5) mL of ice-cold DPBS was added to each petri dish prior to filtering each cell suspension through a fresh 40 µm nylon mesh into respectively labeled 15 mL conical tubes on ice using a fresh 10 mL serological pipette for every sample. Filtered samples were centrifuged at 400 x g (max RCF) for 10 minutes at 4°C. Cell supernatants were aspirated and each pellet was resuspend in 4 mL of a 1X ACK lysing buffer using a fresh 5 mL serological pipette for each sample to avoid cross-contamination. Samples were placed on ice for 5 minutes to lyse RBCs. Tissue samples were centrifuged at 400 x g (max RCF) for 10 minutes at 4°C, had their supernatants aspirated, and their cells resuspended in flow buffer + azide using the

following volumes: 1000 μL for thymi; 1000 μL for spleens; 200 μL for bone marrow; 100 μL for deep/superficial cervical lymph nodes.

Blood samples were next lysed by adding 10 mL of 1X ACK lysing buffer to each 15 mL polypropylene conical tube. Tubes were placed back on ice for 5 minutes (or until blood color changed from dark burgundy to bright red). Blood samples were then centrifuged at 400 x g (max RCF) for 10 minutes at 4°C, their supernatants aspirated, and their WBC pellets resuspended with 200 μL of flow buffer + azide. Samples were stored on ice.

Two (2) μL of each tissue sample were then added to the 198 μL of flow buffer (a 1:100 dilution) in the respectively labeled 0.5 mL microcentrifuge tubes using a P20 micropipette equipped with a gel loading tip. Ten (10) μL of each 1:100 dilution was further diluted 1:1 with a 0.4% trypan blue solution. Ten (10) μL of the resultant solution was then used to estimate cell number using a brightfield microscope and a glass hemocytometer. Typical cell yields were as follows: $3x10^5$ – $1x10^6$ cells from the blood; $3x10^7$ – $8x10^7$ cells from the spleen; $6x10^7$ – $8x10^7$ from the thymus; $6x10^6$ – $1.5x10^7$ from the combined deep/superficial cervical lymph nodes; $9x10^6$ – $1.5x10^7$ from the bone marrow. Cell counts were recorded in an spreadsheet which returned the volume of additional flow buffer + azide required per sample to achieve a final concentration of approximately $2x10^7$ cells/mL (**Supplementary Table 2**). Because mouse blood typically contained less than $2x10^6$ total cells, the 200 μL volume of each blood sample was simply split between the respective experimental well and the CD49b single-positive compensation control well (**see Supplementary Fig. 2e for plate details**).

**Immunolabeling**

The following disposable reagents were gathered and labeled before each of our study's 3 time points:

- 1.5 mL microcentrifuge tubes (12)

    - labeled in duplicate: <target antibody or CD45 isotype>
    - tubes were placed into a microcentrifuge tube rack on ice
- 12-well V-bottom reagent reservoir (1)
    - individual compartments labeled: <target antibody or CD45 isotype>
- 15 mL conical tubes (2)
    - one labeled "cocktail", the other labeled "FVD"
    - placed on ice

Dilutions of each antibody (1:10) were prepared using the 12 microcentrifuge tubes. Refer to accompanying spreadsheet for preparation details (**Supplementary Table 2**). From these 1:10 dilutions, antibodies were further diluted in the respective wells of a 12-well V-bottom reagent reservoir to achieve 100 µL volumes at the final antibody concentration to immunolabel the cells of each single-color compensation control. The remaining 1:10 antibody dilutions were used to prepare a master mix of combined target antibodies (excluding the CD45 isotype) placed in the 15 mL tube labeled "cocktail". All final antibody dilutions were stored on ice in the dark.

One-hundred (100) µL aliquots of each cell suspension were added to the wells of a 96-well V-bottom microplate using a multichannel pipette according to the plate layout specified in (**Supplementary Fig. 2e**). The plate was then centrifuged at 100 x g (max RCF) for 6 minutes at 4°C. Fifty (50) µL of supernatant was aspirated and cells were resuspended with 100 µL of Fc block (15 µg/mL final concentration) the total volume of which was determined using the spreadsheet (**Supplementary Table 2**). Cells were blocked on ice for 5 minutes before being centrifuged at 100 x g (max RCF) for 5 minutes at 4°C. Fifty (50) µL of cell supernatant was aspirated. The 80 experimental tissue samples were resuspended with 91 µL of the combined target antibodies from the tube labeled "cocktail". The 100 µL volumes in the 12-well V-bottom reagent reservoir were added to the respective

single-color compensation control wells; CD45 isotype antibodies were added to the "ISO" well. Cells in the "UNS" and "FVD" wells were resuspended with 91 µL of Brilliant Stain Buffer. The microplate was allowed to incubate on ice in the dark for 15 minutes before adding 100 µL of DPBS to each well and mixing thoroughly with a multichannel pipette. The plate was then centrifuged at 100 x g (max RCF) for 5 minutes at 4°C followed by aspirating 191 µL from each well. Two-hundred (200) µL of DPBS were added to each well using a multichannel pipette and mixed thoroughly by pipetting. The plate was centrifuged at 100 x g (max RCF) for 5 minutes at 4°C followed by a 200 µL aspiration of supernatant. Fixable viability dye was diluted 1.5:1,000 in 1X DPBS in the 15 mL conical tube labeled "FVD" according to the spreadsheet (**Supplementary Table 2**). One-hundred (100) µL of the diluted FVD were added to each well (a 1:1,000 final dilution) except for the "UNS", which was resuspended with 100 µL of DPBS only. Cells were incubated on ice in the dark for 30 minutes. One-hundred (100) µL of DPBS were then added to each well and with a multichannel pipette and pipetted thoroughly to wash. The plate was centrifuged at 100 x g (max RCF) for 5 minutes at 4°C followed by a 200 µL aspiration, addition of 200 µL of DPBS using a multichannel pipette, and through mixing. The plate was centrifuged at 100 x g (max RCF) for 5 minutes at 4°C followed by a 200 µL aspiration.

One-hundred (100) µL of a fixation/permeabilization solution were next added to each well and immediately resuspended with a multichannel pipette to prevent cell-to-cell crosslinking. Cells were incubated on ice in the dark for 20 minutes followed by the addition of 100 µL of flow buffer and thorough mixing with a multichannel pipette. The plate was centrifuged at 100 x g (max RCF) for 5 minutes at 4°C followed by a 200 µL aspiration and resuspension with 200 µL of flow buffer. A Microseal 'F' foil seal was applied to the top of the 96-well microplate to prevent dehydration, wrapped in aluminum foil to block light, and stored at 4°C prior to data acquisition by flow cytometry.

**PMT Calibration**

Detection channel PMT voltages were calibrated such that the signal intensity distribution corresponding to background autofluorescence of FVD-labeled splenocytes was on scale and to the left of center. FVD-labeled single-color compensation control splenocytes were run to verify that the assigned PMT voltages were compatible with the dynamic range of each immunomarker's expression profile (i.e. that immunopositive cells were on scale). To prevent downstream compensation values from exceeding 100%, optical spillover of each single-color compensation control into off-target detection channels was checked to ensure that peak signal intensity occurred in the target detection channel. Sphero Rainbow Fluorescent Particles (single-positive beads) were run to predefine tolerability ranges for laser intensity, stability, and alignment before initiating our study so that changes in laser emission power could be monitored and accounted for between successive data acquisitions to prevent run-to-run variation. Single-positive beads were gated according to the following strategy:

- FSC-A vs. SSC-A: on single-positive beads
- biexponential histograms of all detection channels
    - An interval gate was placed around the peak in each detection channel to define a narrow tolerability range to calibrate to between runs.

**Data Acquisition**

Cytometer setup & tracking was performed using FACSDiva CS&T research beads to optimize and standardize instrument performance prior to each data acquisition. The 96-well V-bottom plate containing the 80 immunolabeled experimental tissue samples and 16 optical controls was then loaded into a BD HTS affixed to a BD LSR II SORP flow cytometer. The gating strategy used at each acquisition was as follows:

- FSC-A vs. SSC-A: on all events (minus RBCs/debris)
- SSC-H vs. SSC-W: doublet discriminator
- FSC-H vs. FSC-W: doublet discriminator
- BUV395-A (FVD) (detected with 355 nm laser off of a 450/50 band pass filter) vs. FSC-A: on FVD negative cells (i.e. viable cells)
- biexponential histograms of all detection channels
    - laser line, band pass filter, long pass filter, antibody detected:
        - 405 nm, 525/50, 505, V500-CD45
        - 488 nm, 710/50, 690, PerCP/Cy5.5-CD45R/B220
        - 355 nm, 740/35, 690, BUV737-CD11b
        - 594 nm, 660/20, 640, Alexa Fluor 647-CD11c
        - 488 nm, 525/50, 505, Alexa Fluor 488-CD3ε
        - 405 nm, 670/35, 635, BV605-CD4
        - 488 nm, 780/60, 755, PE/Cy7-CD49b
        - 488 nm, 610/20, 600, PE-CF594-CD8α
        - 488 nm, 575/26, 505, PE-F4/80
        - 594 nm, 780/60, 735, APC/Cy7-Ly6C
        - 405 nm, 780/60, 750, BV711-Ly6G

Samples were run in the following order (**see Supplementary Fig. 2e for plate details**):

1. SP beads (PRE): to check that PMT voltages were within previously defined tolerability ranges prior to data acquisition.
2. unstained control splenocytes (UNS)
3. unstained control splenocytes labeled with FVD (FVD)

4. control splenocytes labeled with FVD and CD45 isotype control antibodies (ISO)
5. single-color compensation controls stained with FVD (control splenocytes were used for each antibody except CD49b, in which case WBCs were used due to the increased abundance of $CD49b^+$ cells in blood)
6. experimental samples (16 mice x 5 tissue samples = 80 total)
7. SP beads (POST): to check that PMT voltages remained stable over the acquisition period (fluidic anomalies can impact laser delay stability)

Raw data were exported as FCS3.0 files upon completion of each data acquisition session.

**Spectral Deconvolution and Data Cleanup**

FlowJo software was used to spectrally deconvolve raw flow cytometry data. Data from 15 of the 16 optical control wells (UNS was excluded) were imported into the *compensation group* of a new FlowJo *workspace*. CD45 signal intensity distributions were invariably unimodal making it difficult to objectively define a compensation gate for the CD45 single-positive control alone. Thus, the data corresponding to well E11 (ISO) was merged with that of F9 (CD45 single-color compensation control) using FlowJo's *concatenate* feature. The merged data were saved as a new FCS3.0 file and imported into the *compensation group* of the current *workspace*. The original CD45 single-positive compensation control and ISO samples were then deleted from the *workspace*. The merging procedure resulted in a bimodal distribution and the ability to objectively define a CD45 compensation gate between its two peaks. The merged CD45 file plus the other 10 single-color compensation controls and the FVD well (E10)—which served as the compensation control for the for the FVD itself—were gated for viable singlets according to the following strategy:

- FSC-A vs. SSC-A: on all events (minus RBCs/debris)

- SSC-H vs. SSC-W: doublet discriminator
- FSC-H vs. FSC-W: doublet discriminator
- BUV395-A (FVD) vs. FSC-A (viewed as a contour plot at the 2% level): on FVD negative cells (i.e. viable cells)
- backgate to FSC-A vs. SSC-A: on total viable singlets (or a subset for scarce populations)

Once gated, viable singlets of each compensation control sample were visualized as histograms in their respective detection channel. Signal intensity values of each histogram were bisected at the interface of the penultimate and ultimate modes of each signal intensity distribution using FlowJo's *bisector tool*. Its *compensation* tool was then opened and the subsets to the left and right of the bisection were dragged into fields labeled *negative* and positive, respectively. The process was repeated for all 11 antibodies plus the FVD. Next, a new *group* in the *workspace* window was generated and titled "cocktails" to which the 80 experimental samples were imported. The finalized compensation matrix was then applied to the "cocktails" group. Viable singlets from each experimental sample were gated in the same way as the single-color compensation controls according to the first 4 steps of the gating strategy outlined above then exported as new FCS3.0 files; the aggregate of such files from each of the study's 3 time points served as input into our computational data analysis algorithm.

**Weighted Random Sampling**

A 10 million cell weighted random sample (WRS) was derived from the cleaned flow cytometry data to help balance the number of cells per tissue sample. Sample weights were defined per tissue per cell according to the formula $[(1/\omega) \times (1/N_i)]$ where $\omega$ was the number of unique tissue types (5 in this cases) and $N_i$ was the number of events associated with the $i^{th}$ tissue where $i$ took the categorical values blood, marrow, nodes, spleen, thymus.

**Histogram Gating**

Cleaned flow cytometry data (i.e. compensated viable singlets) were displayed as 2,640 histograms (240 samples x 11 antibody detection channels) plotted on a Logicle[70] scale and formatted as scalable vector graphics (SVGs) in the context of a scrolling HTML table viewable with a web browser. A KDE of the signal intensity distribution of cells from the FVD well (i.e. compensated unstained viable splenocytes) was superimposed on each to identify signal intensity values corresponding to autofluorescence background. This allowed for the rapid recording of bisection point at the interface of the first (autofluorescence) and second (true signal) peaks for all histograms in a .TXT file. A vertical line was then programmatically rendered at the location of each bisection point and again visualized as a scrolling HTML table on the web for confirmation or refinement. The numerical value of each bisection point was then Logicle-transformed and subtracted from the Logicle-transformed signal intensity values of its corresponding histogram (i.e. Logicle[data $point_i$]) – Logicle[bisection point]) resulting in the Logicle-transformed bisection point assuming the numerical value of zero and background signal intensity values becoming negative valued. Since the 5 lymphoid tissue types predominately consisted of immune cells, the CD45 signal intensity distributions were invariable unimodal with no discernable local minima. Thus, for each time point and tissue combination, a common CD45 bias was curated by pooling the corresponding samples, computing Q25 – [1.5 * [Q75 - Q25]], then rounding to the nearest multiple of 5. (where Q25 and Q75 were the first and third quartiles of the Logicle-transformed data, respectively).

Immunophenotypes interpreted as $CD49b^+$ granulocytes were identified in the blood of both control and GBM mice. Since granulocyte interaction with $CD49b^+$ platelets is a described phenomenon thought to represent a physiologic process required for neutrophil extracellular trap formation[71,72], we

considered these cells as a likely artifact of residual platelets present within blood samples. In taking a conservative approach to correct for this discrepancy, cell status of the CD49b immunomarkers was only considered in cases where the immunophenotype was otherwise consistent with NK cells (e.g. $CD45^+$, $CD49b^+$, $CD11b^+$). Thus, a Boolean truth value of zero for the CD49b channel was uniformly applied to all cells whose immunophenotype was not matching NK cells.

**t-CyCIF**

The reader is referred to www.cycif.org for detailed instruction t-CyCIF methodology[54]. Briefly, 5µm-thick FFPE tissue sections of the tumor-ipsilateral brain hemisphere of a C57BL/6J mouse engrafted with $3x10^4$ GL261 cells 36-days prior was serially scanned using 2x2 binning with a CyteFinder slide scanning fluorescence microscope (RareCyte, Seattle, WA, USA) equipped with a 40X (0.6NA) long working distance objective on each of 4 imaging cycles. Before immunolabeling with the first set of 3 fluorophore-conjugated antibodies, the tissue was counterstained with DAPI at a 1:3,000 dilution of a 10 mg/mL stock in 1x PBS for 15 minutes at RT then blocked with Odyssey Blocking Buffer at RT for 1 hour to limit non-specific antibody binding. Blocked slides were then imaged to document background autofluorescence prior to immunolabeling. Antibody incubations were performed at 4°C overnight in an opaque and humidified chamber. After immunolabeling, slides were washed 3 times with 1x PBS, temporarily coverslipped in 1x PBS containing 10% glycerol, and re-imaged. Immediately after imaging, slides were de-coverslipped by vertical submersion in Coplin jars containing 1x PBS until the coverslip spontaneously fell way from the slide. Antibody fluorescence was deactivated by submersion of the slide in a 3% $H_2O_2$ solution containing 20 mM NaOH in 1x PBS for 2 hours at RT in the presence of intense fluorescent light. Following fluorophore deactivation, slides were rinsed briefly in 1x PBS, then subject to the next round of immunolabeling.

Upon completion of the cyclic imaging procedure, autofluorescence background was computationally subtracted on a pixel-by-pixel basis using ImageJ. The final 12-plex mosaic image was generated by aligning (or registering) the 168 400x300µm imaging fields acquired during each imaging cycle on their DAPI counterstained nuclei using ImageJ's Multistack Registration Plugin. Registered images were compiled into multi-image stacks and segmented based on the DAPI signal acquired during the last imaging cycle by applying a uniform threshold on the DAPI channel across all images and then converting this signal into binary regions of interest (ROIs) using the ImageJ's *Analyze Particles* function. ROIs corresponding to single-cell nuclei were enlarged by 3 pixels to cover immune cell cytoplasm and membrane. Respective ROIs where overlaid on each image to obtain integrated fluorescence signal intensity data on each cell for across all 12 immunofluorescence channels.

**RNA-seq**

The spleens of five 12-week-old tumor-naïve C57BL/6J mice were immunodepleted of B cells using MojoSort mouse CD19 nanobeads (Biolegend, Cat. No. 480002) before FACS-purifying $B220^+$ $CD3\varepsilon^+$ $CD8\alpha^+$ (i.e. $B220^+$ CD8T cells) and $B220^-$ $CD3\varepsilon^+$ $CD8\alpha^+$ (i.e. CD8T cells) into respective 15 ml conical tubes containing ice-cold with 0.5% BSA DPBS. Approximately $1x10^6$ cells of each type were centrifuged at 400 x g (max RCF) for 10 minutes at 4°C and resuspended in RLT lysis buffer prior to total RNA extraction with Qiagen's RNeasy mini kit using the optional DNase treatment (Qiagen, Cat. No. 74104). Total RNA was then used to prepare sequencing libraries of the coding transcriptome using Illumina's TruSeq stranded mRNA protocol. Libraries were sequenced by synthesis on a Nextseq 500 instrument. Fastq files were processed on a high-performance computer cluster using a standardized data analysis pipeline involving the analysis programs FASTQC, STAR, Salmon, featureCounts, EdgeR,

Kallisto. Kallisto transcript abundance files were then analyzed on a desktop computer using the Sleuth RNA-seq analysis program[49].

**Software**

- FACSDiva (version 8.0)
- FlowJo (version 10.3.0)
- Python (version 3.6.1)

**Statistics**

Statistical tests were performed using SciPy.stats, a Python-based library of validated statistical functions. Statistical tests used throughout this paper are described at their point of reference. Two-sample hypothesis tests were considered statistically significant if their FDR adjusted p-value (or q-value) reached a cutoff of $\leq 0.05$.

**Data and Code Availability**

SYLARAS source code and the cleaned GBM flow cytometry dataset are freely available for download at www.sylaras.org.

**FIGURE LEGENDS**

**Figure 1** Workflow for systemic immunophenotyping of GBM-bearing mice by 12-color flow cytometry. *(1)* GBM cell suspension or vehicle alone was stereotactically-injected into the striata of age-matched cohorts of 24 mice. *(2)* Lymphoid tissues of 8 mice per treatment group were harvested at days 7, 14, and 30-days after the engraftment procedure. *(3)* Tissues were processed into single-cell suspensions and plated in a 96 well V-bottom plate (see Supplementary Fig. 1h for details on optical controls). *(4)* Cells were immunolabeled with a cocktail of 11 fluorophore-conjugated antibodies followed by incubation with a fixable viability dye (FVD). *(5)* Single-cell data were acquired by high-throughput flow cytometry. *(6)* Raw data files were spectrally deconvolved and gated for viable singlets. *(7)* Cleaned data underwent a computer-assisted unidimensional gating procedure (see Fig. 2 for details) prior to being computationally analyzed by the SYLARAS data analysis pipeline.

**Figure 2** Systematic cell subset identification via computer-assisted unidimensional gating. (**a**) Logicle-displayed signal intensity histograms for two hypothetical antibody detection channels (IM1=green, IM2=blue). (**b**) Tabular data structure for recording histogram gate values on a replicate, tissue, condition, time point, and detection channel basis. (**c**) Histograms shown in panel (a) after SYLARAS renders a vertical line at the gate value for rapid gate confirmation or refinement. (**d**) Histograms shown in panels (a and c) after programmatic subtraction of their gate values from the values in their corresponding signal intensity distribution. Note how the procedure causes the zero point of each distribution to become zero-centered at the signal-to-noise interface.

**Figure 3** Mouse lymphoid tissue architecture characterized in 30 cellular immunophenotypes. (**a**) Sunburst plot of the hierarchical organization of a dictionary-based immunophenotype classification

scheme. Standard cell classes are represented by the plot's inner wedges whose expressed antigens are indicated at the center of the plot (except for DC, ISPT, NK, Precursor, LTi to avoid text overlap). Outer wedges represent variants of each landmark class whose aliases are prefixed according to conventional +/- immunophenotyping notation. (**b**) Heatmap diagram of the 11-dimensional Boolean vector associated with all 30 immunophenotypes characterized in this study. Also shown is the percentage of the 10M cell WRS accounted for by each immunophenotype (left) and their presumed cell type identity (right) (**c**) Immunophenotype FSC and SSC distributions shown for control (Ctrl, blue) and GBM-burdened (GBM, green) mice. FSC low/high cutoff = 35,000; SSC low/high cutoff = 97,000. Immunophenotypes are shown in ascending rank order from left-to-right according to the median value of the control group. Box plot elements: horizontal line, median; box limits, first to third quartile (Q1 to Q3); whiskers, from Q1-1.5 x interquartile range (IQR) to Q3 + 1.5 x IQR; diamond points, outliers. (**d**) Bar and stair plots showing the individual (bars) and cumulative (steps) contribution of successive immunophenotypes in accounting for the percentage of each of 5 mouse lymphoid tissue types. (**e**) Stacked bar chart showing the fraction of each immunophenotype across 5 mouse lymphoid tissue types (top x-axis) listed in ascending rank order along the y-axis according to their information entropy (superimposed dashed line, bottom x-axis). (**f**) Average antigen expression level of 30 Phenograph clusters obtained after running the algorithm using k=20 nearest neighbors and the Euclidian distance metric on an 8K cell subsample of the full dataset. Also shown is the percentage of the subsample accounted for by each cluster (left) and the information entropy associated with their cell type composition as determined by our dictionary-based immunophenotype classification scheme (right). The most populous dictionary immunophenotype accounting for the majority $\geq$50% of each cluster are indicated along with a categorical score of agreement between knowledge-based and data-driven cell subset identification.

**Figure 4** SYLARAS reveals GBM-induced perturbation in the frequency of peripheral immune cell subsets hitherto undescribed in the disease. (**a**) Weighted $\log_2$ fold-change in time and tissue-specific immunophenotype frequency between GBM-bearing and age-matched, mock-engrafted control mice (GBM/Ctrl). Icons denote one of three different q-value ranges. (**b**) Mean difference in the absolute magnitude of time and tissue-specific immunophenotype frequency between GBM-bearing and age-matched, mock-engrafted control mice (GBM - Ctrl). (**c**) SYLARAS dashboard of the $B220^+$ CD8T immunophenotype revealing 10 attributes: *(1)* dictionary alias; *(2)* major immune lineage; *(3)* condition-specific FSC and SSC distributions; *(4)* Logicle-transformed immunomarker signal intensity distributions; *(5 and 6)* time and tissue-specific mean difference (left) and $\log_2$ fold-change (right) between GBM-burdened and control mice (n=8 mice/group/tissue/time point Icons denote one of three different q-value ranges; *(7)* color-coded tissue distribution (the same as in attributes 5 and 6); *(8)* fraction of the 10M cell WRS accounted for by the immunophenotype; *(9)* percentage of 5 lymphoid tissues accounted for by the immunophenotype across the study's 48 mice; *(10)* priority rank—a metric of the measurability and statistical significance of GBM-induced effect size calculated as $[1-q]^3 \times |R + \Delta| + \sigma)$ where q = q-value, $R = \log_2(0.01 + \text{mean GBM \%} / 0.01 + \text{mean Ctrl \%})$, $\Delta = (\text{mean GBM \%} - \text{mean Ctrl \%})$, and $\sigma$ = number of time points a given cell type was involved in a statistically significant difference between the two treatment groups.

**Figure 5** Analysis of mouse-to-mouse variation in immunophenotype frequency provides network-level insight into GBM's immunoregulatory control over the peripheral immune system. (**a**) Score plot of the first 2 PCs of a PCA where the input was a n x m data matrix of the percentage of the study's 240 tissue samples (rows) accounted for by each of 30 immunophenotypes (columns). Circles highlight outlier

samples from late-stage GBM-burdened mouse 3. (**b**) Clustermaps showing the $\log_2$ ratio between the tissue-specific immunophenotype frequency for each late-stage GBM-burdened mouse (columns) and the median value for the group of 8 mice. Significant outliers indicated by red text. Clustering was performed using the unweighted pair group method with arithmetic mean (UPGMA) linkage and Euclidean distance. (**c**) Percentage of Ly6C$^-$ PMN cells in the bone marrow of each of the study's 48 mice. Late-stage GBM-burdened mouse 3 is indicated. (**d**) T-tests (computed across rows; experimental conditions) and Spearman's rank-order correlation (computed across columns; immunophenotypes) demonstrating that statistically significant co-variation among biological replicates of the same experimental condition can arise independently of significant differences in population average values of different experimental conditions. (**e**) Seven (7) statistically significant time and tissue-specific Spearman's rank-order correlations in immunophenotype frequency. Asterisk denotes the correlation pair shown in the top row of panel (d). (**f**) Schematic diagram of correlation profile clustering. Positive correlation = red, negative correlation = blue, identity correlation = grey. Clustering tissue-specific immunophenotypes are presumptively co-regulated while anti-correlated clusters are presumed to be functionally-antagonistic. (**g**) Agglomerative hierarchical clustering of Spearman's rank-order correlation coefficients computed across biological replicates of control (left) and GBM-burdened (right) mice regardless of time point. Clustering was performed using the UPGMA linkage algorithm and Euclidean distance using only immunophenotypes with a frequency >0.1% across replicates. Clusters have been color-coded independently for in each treatment group. Members of GBM-burdened cluster 3 are specified in order from top-to-bottom.

**Figure 6** B220$^+$ CD8T cells are a transcriptionally-distinct subset of CD8$^+$ T lymphocytes. (**a**) Scatter plot stratifying CD8T, B220$^+$ CD8T, CD4T, and B cells in the the blood of the study's 24 control mice

according to their expression of B220 and CD8α. (**b**) Percentage of CD8T cells and $B220^+$ CD8T cells in the thymus of the study's 48 mice. (**c**) Heatmaps of the mean $\log_2$ fold-change in CD8T (left) and $B220^+$ CD8T cell (right) frequency between GBM-burdened and age-matched, mock-engrafted control mice (n=8 mice/group/tissue/time point). Icons denote one of three different q-value ranges. (**d**) Regression plots showing the frequency of $B220^+$ CD8T cells (x-axes) relative to CD8T cells (y-axes) in the spleen of control (left column) and GBM (right column) mice during each of the study's three time points (rows). Data points represent 8 replicate mice. Regression plot elements: line, regression line; transparency, 95% confidence interval for the regression; $R^2$, coefficient of determination. (**e**) Gating strategy for the FACS-purification of $B220^{hi}$ and $B220^{lo}$ CD8T cells from the CD19-immunodepleted, tumor-naïve, C57BL/6 mouse spleen. (**f**) Scree plot showing the percentage of explained variance accounted for by individual (bars) and cumulative (stairs) PCs from a PCA performed on normalized mRNA transcript counts table of $B220^{hi}$ (n=2) and $B220^{lo}$ (n=3) CD8T cells. (**g**) PC1 vs. PC2 score plot. Samples are color-coded by immunophenotype; biological replicates are indicated by number. (**h**) mRNA transcripts with the top 5 contribution scores for PC1 (left) and PC2 (right). (**i**) Table of transcripts differently expressed between $B220^+$ CD8T and CD8T cells; transcripts of interest are highlighted. b = beta-value (approximate fold-change).

**Figure 7** B220+ CD8T cells are a morphologically and spatially-distinct subset of GBM-infiltrating $CD8^+$ T lymphocytes. (**a**) Spatial coordinates of cells composing a 5-µm thick slice of the tumor-ipsilateral brain hemisphere of a GL261-bearing mouse 36-days after tumor engraftment. Tumor area is outlined by the black dashed perimeter and characterized by high cell density compared to normal tissue constituting the cerebral cortex. (**b**) Cell counts for the 7 most frequent immunophenotypes identified in the late-stage GL261 GBM TME. An thumbnail example of a cell bearing each immunophenotype is

shown. Antibody clones used in the immunolabeling are indicated in the banner across the top of the panel. (**c**) Examples of CD8α single-positive and B220/CD8α double-positive cells within the GL261 TME. Tile coordinates of each cell permit cross-referencing with the full-resolution PDF provided as Supplementary Fig. 7. (**d**) Box plot distributions of Logicle-transformed CD8α signal intensity from CD8T (left) and B220$^{+}$ CD8T cells (right) in the blood of the study's 24 control mice. (**e**) KDEs (concentric black contour lines) of the cellular density for the 7 abundant immune subsets identified in the TME superimposed on the same scatter plot of vimentin$^{+}$ lineage$^{-}$ tumor cells colored-coded according to cell density relating immune cell spatial distribution with tumor cell density. (**f**) Clustermap of the correlation in spatial distribution of the 7 abundant immunophenotype and tumor cells comprising the TME. The minimal overlap observed between B220$^{+}$ CD8T cells and CD8T cells is indicated by the red box

**Figure 8** Identification of a B220$^{+}$ CD8T cell analogue in human blood clinical GBM. (**a**) Representative 20x image of normal human WBCs affixed to a glass microscope slide and immunolabeled with anti-human antibodies targeting CD3δ (green), CD8α (red), and CD45R (blue). (**b**) Counts of the top 6 most abundant cellular immunophenotypes present in the WBC preparation exemplified in panel (a). (**c**) Low-resolution, 4-color mosaic micrograph of a human brain tumor TMA showing (316) core biopsies (each 0.6mm in diameter) from 173 different human brain tumor patients immunolabeled with antibodies targeting anti-human CD45R, CD3δ, and CD8α. (**d**) TMA metadata map showing patient ID (# above each core), number of triple-positive cells (heatmap intensity), and tissue status: primary tumor, recurrent tumor, or tonsil (positive controls for immunolabeling). (**e**) Example core imaged at 20x demonstrating the presence of a triple-positive CD45R$^{+}$, CD3δ$^{+}$, CD8α$^{+}$ T lymphocyte (white box and inset). CD3δ single-positive and CD8α/CD3δ double-positive cells are also

indicated. (**f**) Representative 40x micrographs of CD45R/CD3δ/CD8α triple-positive T lymphocytes in various core biopsies of the TMA shown in panel (c).

**Supplementary Figure 1** Experimental optimization and quality control for 12-color immunophenotyping by flow cytometry. (**a**) 8 point, 2-fold serial dilution titration curves for each fluorophore-conjugated antibody used in the study. Splenocytes from 12-week-old female C57BL/6J mice were used as cells for immunolabeling. The separation index (SI) was calculated as $[MFI_{pos}-MFI_{neg}]/[[84\%_{neg}-MFI_{neg}]/0.995]$, where $MFI_{pos}$ = median fluorescence intensity of the first positive peak, $MFI_{neg}$ = median fluorescence intensity of the autofluorescence peak, $84\%_{neg}$ = $84^{th}$ percentile of the autofluorescence peak as previously described[69]. Cubic splines were used to interpolate adjacent data points. Antibody concentrations yielding peak separation indices are indicated by a green dot. Data acquisition gating strategy: (FSC-A vs. SSC-A) → (SSC-H vs. SSC-W) → (FSC-H vs. FSC-W) → (DAPI-A vs. FSC-A) → (specific antibody vs. count). (**b**) Signal intensity distributions of splenocytes from 12-week-old female C57BL/6J mice immunolabeled with the 11 antibodies indicated in panel (a) plus a fixable viability dye (FVD) as detected in the 12 optical channels of a BD LSR II flow cytometer. Pre- and post-compensation conditions are shown. Antibodies (rows) are color-coordinated with their respective detection channel (columns). Histograms forming the left-to-right downward diagonal across the matrix show the location of the respective channel's compensation gate (blue/green interface). (**c**) Kaplan-Meier survival curve of 10 C57BL/6J mice intracranially engrafted with $3x10^4$ syngeneic GL261 GBM cells at 12-week-of-age. Median survival indicated by intersecting dashed red lines. (**d**) Settings for the cytometer setup & tracking and PMT calibration beads used to standardize cytometer performance across 3 consecutive data acquisitions. (**e**) Cytometer settings. (**f**) Configuration diagrams of the BD LSR II cytometer long-pass and band-pass filters used in this study. (**g**) High-throughput

sampler (HTS) settings used in the study. (**h**) Well locations of the optical controls run in a 96 well V-bottom plate during each data acquisition. UNS = unstained, FVD = fluorescent FVD only, ISO = CD45 isotype plus FVD, PRE = single-positive beads run before data acquisition, POST = single-positive beads run after data acquisition. (**i**) Radial bar chart showing the percentage of dead cells in the study's 240 tissue samples. C = control, T = GBM. (**j**) Radial bar charts of cell number in each tissue sample from control (left) and GBM (right) mice after a weighted random sampling to help balance the number of cells per sample.

**Supplementary Figure 2** Gate placement for each of the study's 2,640 signal antibody intensity histograms (11 detection channels x 5 tissue types x 48 mice). Kernel density estimates (KDEs) of unstained splenocytes are superimposed (blue outlines). Data for the CD45 channel are shown as box-and-whisker plots. uns = unstained splenocytes, cd45 = splenocytes labeled with CD45 single-color control, cd45i = splenocytes labeled CD45 isotype control antibodies, 0 = experimental data immunonegative for all other immunomarkers, 1 = experimental data immunopositive for at least of the other immunomarkers, all = combined data from 0 and 1.

**Supplementary Figure 3** A comparison of knowledge-based and data-drive cell subset identification on the same dataset subsample. (**a**) Box plot distributions of Logicle-transformed antigen expression of the 30 immunophenotypes identified by SYLARAS and 30 clusters identified by the Phenograph algorithm. In both cases antigen expression is shown side-by-side for control and GBM mice in descending rank order according the median value of the control group. (**b**) Box plot distributions of Logicle-transformed antigen expression showing data for clusters 1, 7, 9, 15, 16, and 18.

**Supplementary Figure 4** Set of 30 SYLARAS dashboards (1 per immunophenotype).

**Supplementary Figure 5** Silhouette analysis identifying appropriate dendrogram linkage thresholds for condition-specific correlation clustermaps shown in Figure 5g. The number of clusters chosen for each clustermap (indicated by a white asterisk) was defined as the greatest number of clusters among which the fraction of members with negative silhouette scores was < 10%; cluster members are indicated at the leafs of each dendrogram.

**Supplementary Figure 7** Validation and application of a 12-color CyCIF antibody panel to survey the late-stage GBM immune landscape. (**a**) 11 antibodies validated on FFPE tissue sections of an inguinal lymph node from a B16 melanoma-bearing C57BL/6 mouse. Merged image is shown at left; thumbnail images of individual channels are shown at right. (**b**) Single-cell data derived from the segmented micrograph showing the fraction of total cells immunoreactive to each antibody. Antibody signal intensity is indicated by the heatmap. (**c**) Full-resolution PDF of a 168-tile, 12-plex mosaic immunofluorescence micrograph of the tumor-ipsilateral mouse brain hemisphere bearing GL261 GBM 36-days after its engraftment acquired with a 40x objective. Tiles are indicated by X/Y coordinate and tile number and are shown in increasing order from the bottom-left to top-right. Immunomarker colors are as follows: Ly6C (orange), CD8α (yellow), CD68 (cyan), B220 (magenta), CD4 (red), CD49b (white), Ly6G (brown), Foxp3 (blue), CD11b (green), Ki67 (pink), Vimentin (violet), DAPI (gray)**.** (**d-f**) Examples of B220/CD8α double-positive cells, CD8α single-positive cells, and several low-abundance cell types from the micrograph shown in panel (c); tile coordinates are provided for cross-referencing.

**Supplementary Table 1** Antibody details and protocol for 12-plex CyCIF on mouse FFPE tissue sections.

**Supplementary Table 2** Excel spreadsheet for calculating the amounts of antibody stock and diluent, fixable viability dye, Fc block, resuspension volume for cell count estimation, and injectable anesthetics.

# Fig. 1

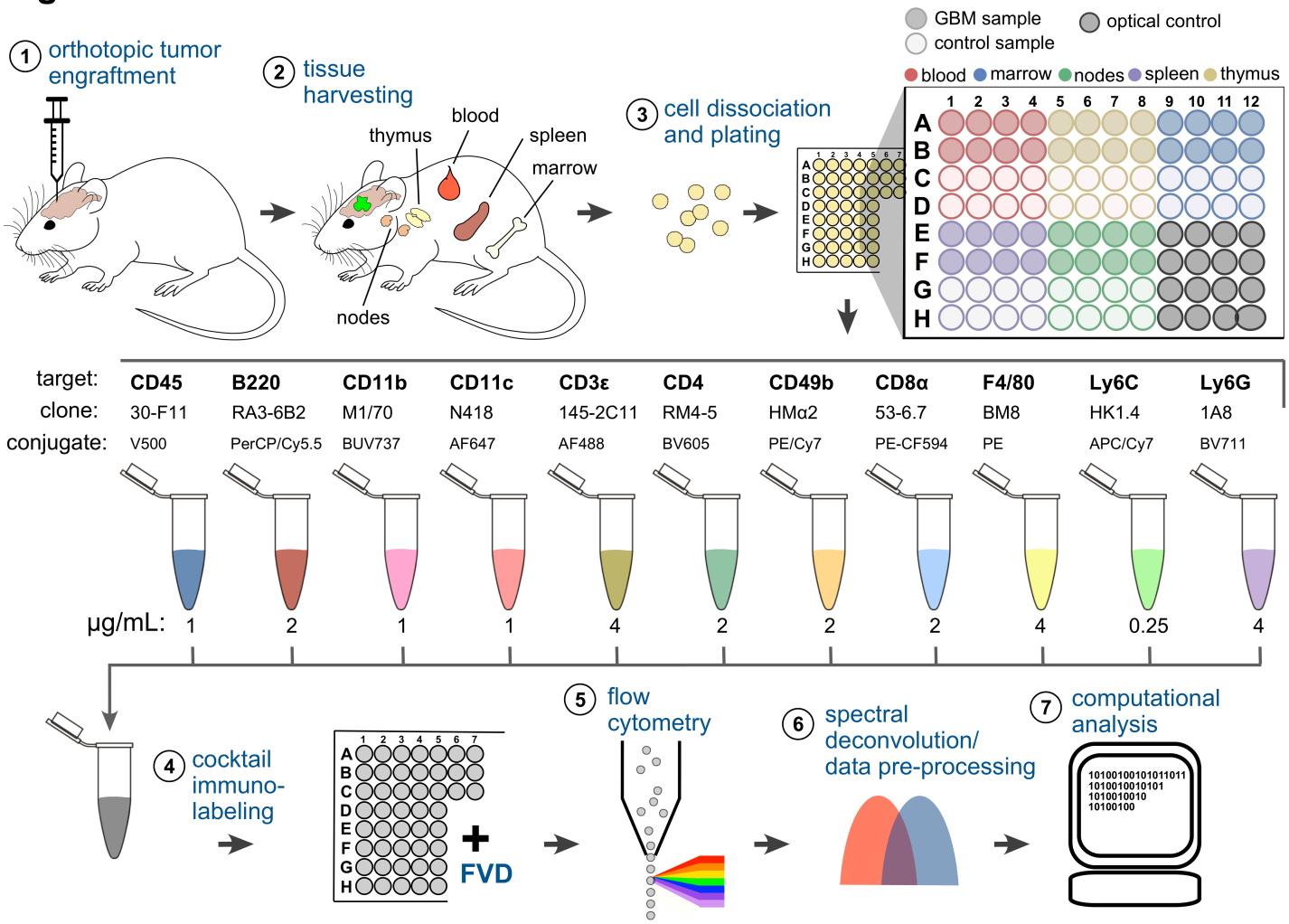
1 orthotopic tumor engraftment
2 tissue harvesting
thymus
blood
spleen
marrow
nodes
3 cell dissociation and plating
GBM sample
control sample
optical control
blood
marrow
nodes
spleen
thymus
target: CD45 B220 CD11b CD11c CD3ε CD4 CD49b CD8α F4/80 Ly6C Ly6G
clone: 30-F11 RA3-6B2 M1/70 N418 145-2C11 RM4-5 HMα2 53-6.7 BM8 HK1.4 1A8
conjugate: V500 PerCP/Cy5.5 BUV737 AF647 AF488 BV605 PE/Cy7 PE-CF594 PE APC/Cy7 BV711
µg/mL: 1 2 1 1 4 2 2 2 4 0.25 4
4 cocktail immuno-labeling
FVD
5 flow cytometry
6 spectral deconvolution/ data pre-processing
7 computational analysis

# Fig. 2

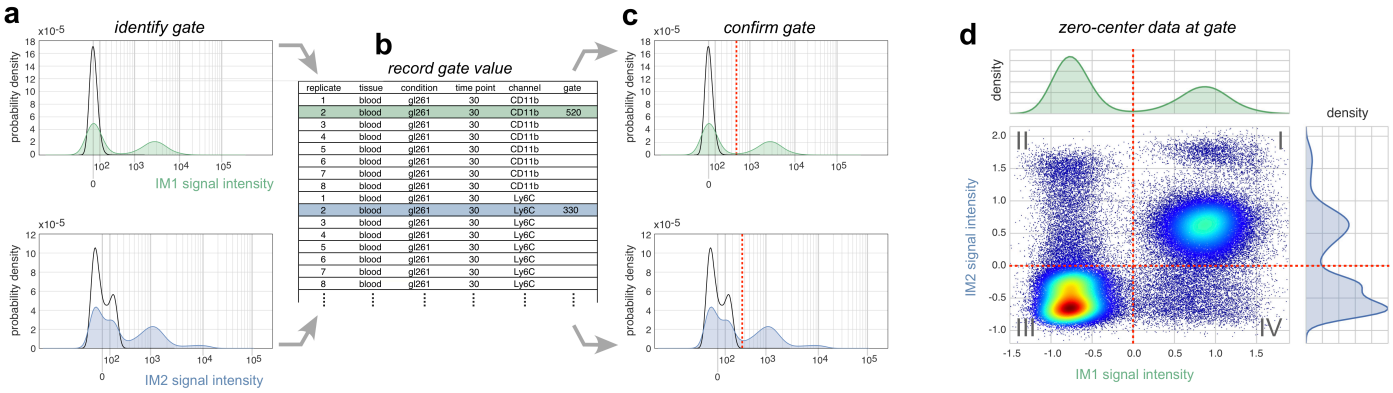


| replicate | tissue | condition | time point | channel | gate |
|---|---|---|---|---|---|
| 1 | blood | gl261 | 30 | CD11b | |
| 2 | blood | gl261 | 30 | CD11b | 520 |
| 3 | blood | gl261 | 30 | CD11b | |
| 4 | blood | gl261 | 30 | CD11b | |
| 5 | blood | gl261 | 30 | CD11b | |
| 6 | blood | gl261 | 30 | CD11b | |
| 7 | blood | gl261 | 30 | CD11b | |
| 8 | blood | gl261 | 30 | CD11b | |
| 1 | blood | gl261 | 30 | Ly6C | |
| 2 | blood | gl261 | 30 | Ly6C | 330 |
| 3 | blood | gl261 | 30 | Ly6C | |
| 4 | blood | gl261 | 30 | Ly6C | |
| 5 | blood | gl261 | 30 | Ly6C | |
| 6 | blood | gl261 | 30 | Ly6C | |
| 7 | blood | gl261 | 30 | Ly6C | |
| 8 | blood | gl261 | 30 | Ly6C | |
| ⋮ | ⋮ | ⋮ | ⋮ | ⋮ | ⋮ |

# Fig. 3

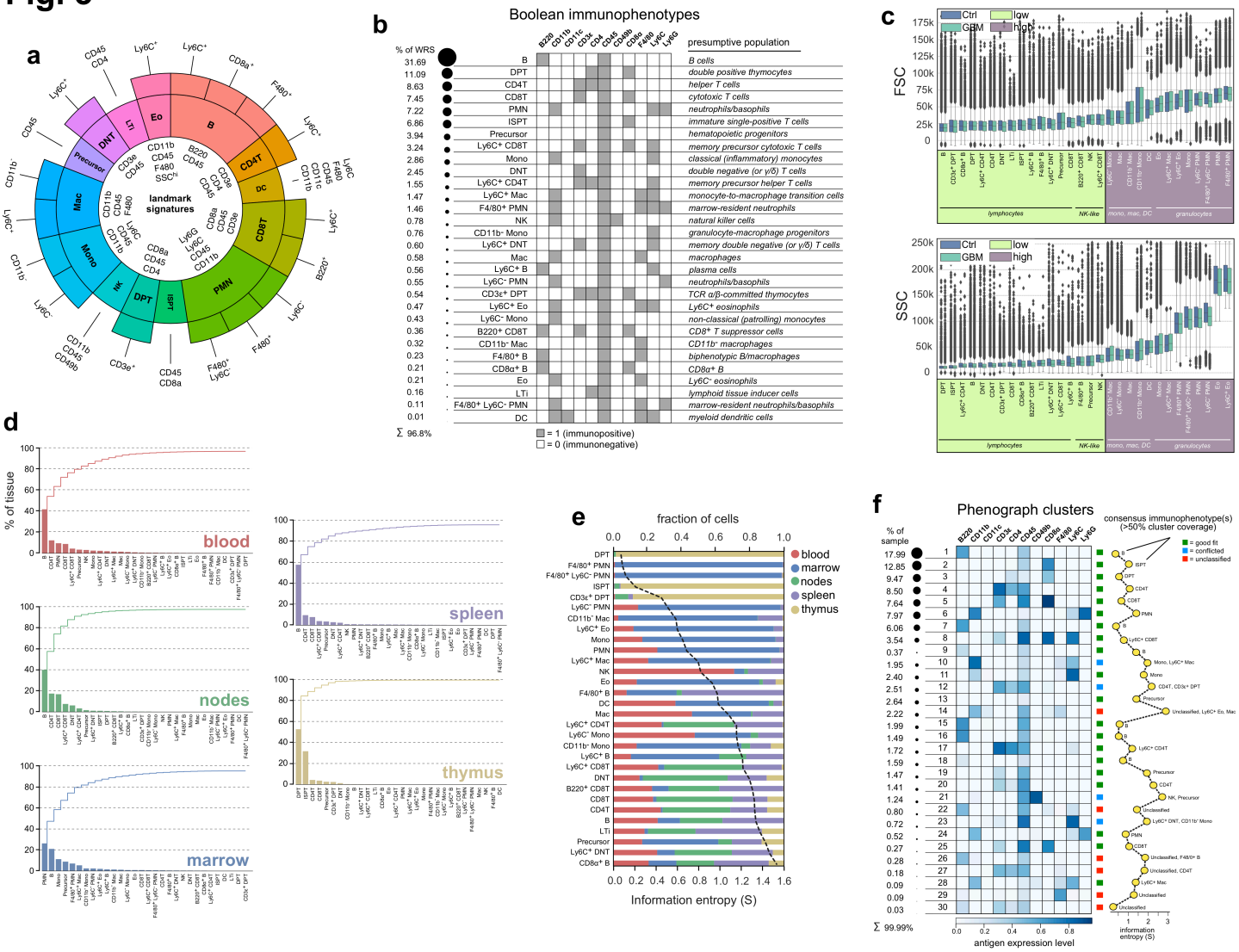
a
landmark signatures
B
CD4T
CD8T
PMN
ISPT
DPT
NK
Mono
Mac
Precursor
DNT
LTi
Eo
DC
b
Boolean immunophenotypes
% of WRS
presumptive population
B cells
double positive thymocytes
helper T cells
cytotoxic T cells
neutrophils/basophils
immature single-positive T cells
hematopoietic progenitors
memory precursor cytotoxic T cells
classical (inflammatory) monocytes
double negative (or γ/δ) T cells
memory precursor helper T cells
monocyte-to-macrophage transition cells
marrow-resident neutrophils
natural killer cells
granulocyte-macrophage progenitors
memory double negative (or γ/δ) T cells
macrophages
plasma cells
neutrophils/basophils
TCR α/β-committed thymocytes
Ly6C+ eosinophils
non-classical (patrolling) monocytes
CD8+ T suppressor cells
CD11b+ macrophages
biphenotypic B/macrophages
CD8α+ B
Ly6C- eosinophils
lymphoid tissue inducer cells
marrow-resident neutrophils/basophils
myeloid dendritic cells
Σ 96.8%
= 1 (immunopositive)
= 0 (immunonegative)
c
Ctrl
GBM
low
high
FSC
SSC
lymphocytes
NK-like
mono, mac, DC
granulocytes
d
% of tissue
blood
nodes
marrow
spleen
thymus
e
fraction of cells
blood
marrow
nodes
spleen
thymus
Information entropy (S)
f
Phenograph clusters
% of sample
consensus immunophenotype(s) (>50% cluster coverage)
= good fit
= conflicted
= unclassified
Σ 99.99%
antigen expression level
information entropy (S)

# Fig. 4

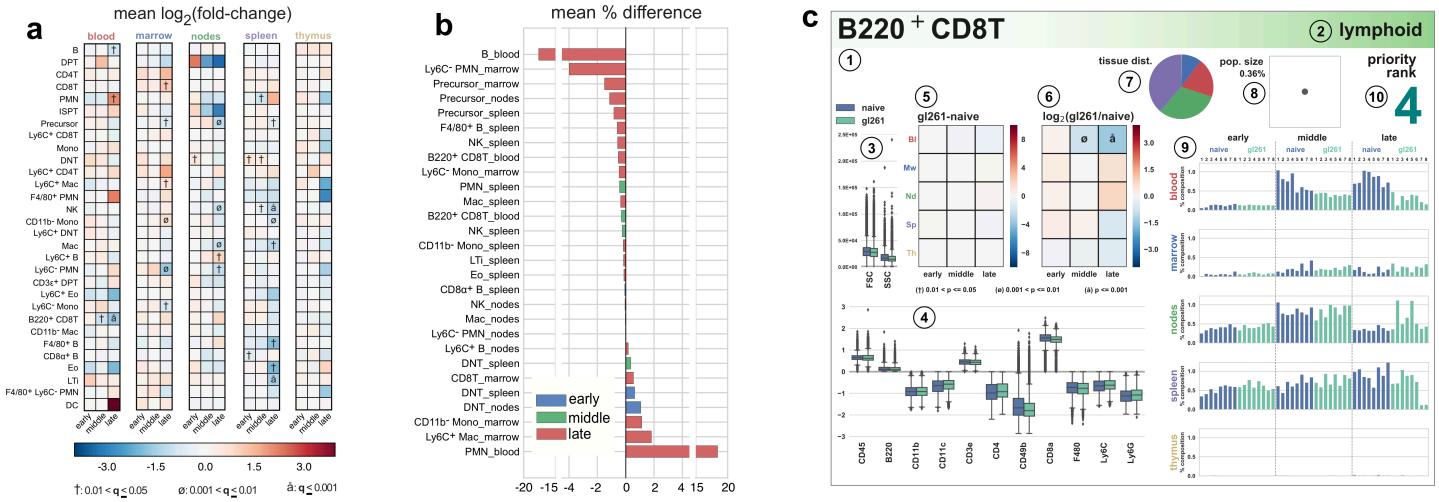
a
mean log2(fold-change)
blood
marrow
nodes
spleen
thymus
early
middle
late
-3.0
-1.5
0.0
1.5
3.0
†: 0.01 < q ≤ 0.05
ø: 0.001 < q ≤ 0.01
å: q ≤ 0.001
b
mean % difference
B_blood
Ly6C- PMN_marrow
Precursor_marrow
Precursor_nodes
Precursor_spleen
F4/80+ B_spleen
NK_spleen
B220+ CD8T_blood
Ly6C- Mono_marrow
PMN_spleen
Mac_spleen
B220+ CD8T_blood
NK_spleen
CD11b- Mono_spleen
LTi_spleen
Eo_spleen
CD8α+ B_spleen
NK_nodes
Mac_nodes
Ly6C- PMN_nodes
Ly6C+ B_nodes
DNT_spleen
CD8T_marrow
DNT_spleen
DNT_nodes
CD11b- Mono_marrow
Ly6C+ Mac_marrow
PMN_blood
early
middle
late
-20 -15 -4 -2 0 2 4 15 20
c
B220+ CD8T
2 lymphoid
1
tissue dist.
7
pop. size
0.36%
8
priority rank
10
4
naive
gl261
5
gl261-naive
6
log2(gl261/naive)
3
Bl
Mw
Nd
Sp
Th
FSC
SSC
early
middle
late
(†) 0.01 < p <= 0.05
(ø) 0.001 < p <= 0.01
(å) p <= 0.001
4
CD45
B220
CD11b
CD11c
CD3e
CD4
CD49b
CD8a
F480
Ly6C
Ly6G
9
blood
marrow
nodes
spleen
thymus
% composition

# Fig. 5

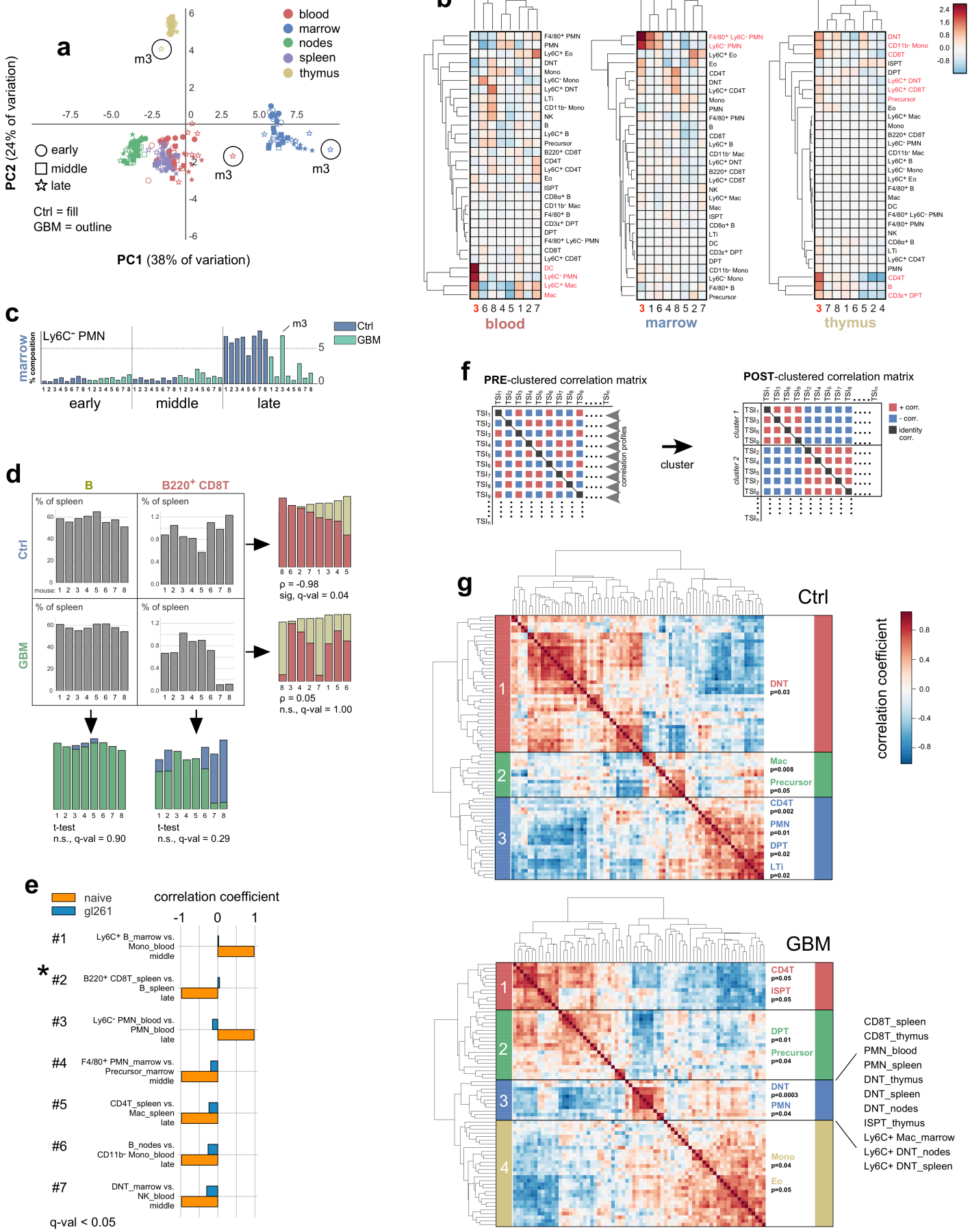
a
blood
marrow
nodes
spleen
thymus
m3
early
middle
late
Ctrl = fill
GBM = outline
PC2 (24% of variation)
PC1 (38% of variation)
b
log2(%rep./%median)
blood
marrow
thymus
c
marrow
% composition
Ly6C⁻ PMN
Ctrl
GBM
m3
early
middle
late
d
B
B220⁺ CD8T
Ctrl
GBM
% of spleen
mouse:
ρ = -0.98
sig, q-val = 0.04
ρ = 0.05
n.s., q-val = 1.00
t-test
n.s., q-val = 0.90
t-test
n.s., q-val = 0.29
e
naive
gl261
correlation coefficient
#1 Ly6C⁺ B_marrow vs. Mono_blood middle
* #2 B220⁺ CD8T_spleen vs. B_spleen late
#3 Ly6C⁻ PMN_blood vs. PMN_blood late
#4 F4/80⁺ PMN_marrow vs. Precursor_marrow middle
#5 CD4T_spleen vs. Mac_spleen late
#6 B_nodes vs. CD11b⁻ Mono_blood late
#7 DNT_marrow vs. NK_blood middle
q-val < 0.05
f
PRE-clustered correlation matrix
POST-clustered correlation matrix
correlation profiles
cluster
cluster 1
cluster 2
+ corr.
- corr.
identity corr.
g
Ctrl
GBM
correlation coefficient
DNT p=0.03
Mac p=0.008
Precursor p=0.05
CD4T p=0.002
PMN p=0.01
DPT p=0.02
LTi p=0.02
CD4T p=0.05
ISPT p=0.05
DPT p=0.01
Precursor p=0.04
DNT p=0.0003
PMN p=0.04
Mono p=0.04
Eo p=0.05
CD8T_spleen
CD8T_thymus
PMN_blood
PMN_spleen
DNT_thymus
DNT_spleen
DNT_nodes
ISPT_thymus
Ly6C+ Mac_marrow
Ly6C+ DNT_nodes
Ly6C+ DNT_spleen

# Fig. 6

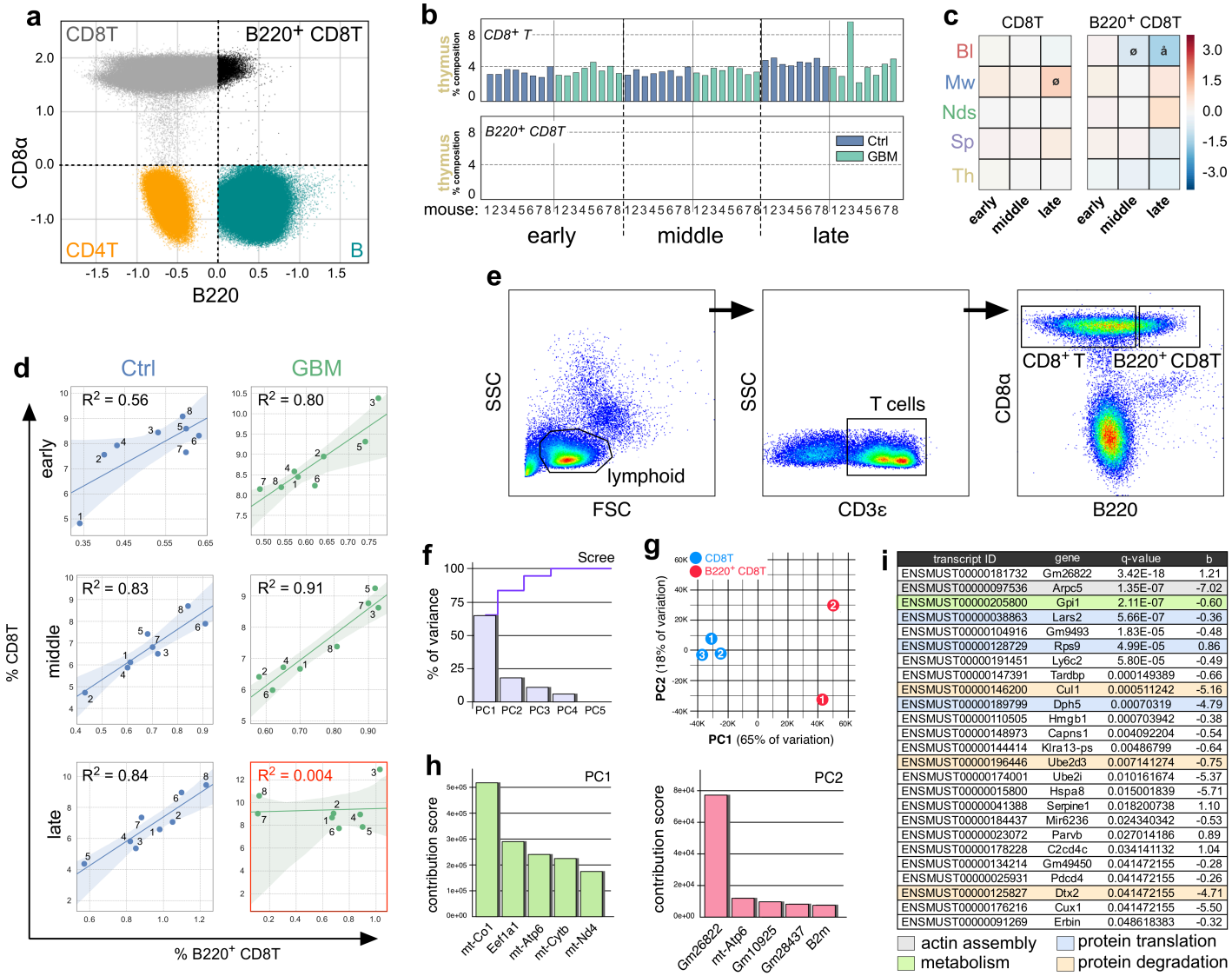


| transcript ID | gene | q-value | b |
|---|---|---|---|
| ENSMUST00000181732 | Gm26822 | 3.42E-18 | 1.21 |
| ENSMUST00000097536 | Arpc5 | 1.35E-07 | -7.02 |
| ENSMUST00000205800 | Gpi1 | 2.11E-07 | -0.60 |
| ENSMUST00000038863 | Lars2 | 5.66E-07 | -0.36 |
| ENSMUST00000104916 | Gm9493 | 1.83E-05 | -0.48 |
| ENSMUST00000128729 | Rps9 | 4.99E-05 | 0.86 |
| ENSMUST00000191451 | Ly6c2 | 5.80E-05 | -0.49 |
| ENSMUST00000147391 | Tardbp | 0.000149389 | -0.66 |
| ENSMUST00000146200 | Cul1 | 0.000511242 | -5.16 |
| ENSMUST00000189799 | Dph5 | 0.00070319 | -4.79 |
| ENSMUST00000110505 | Hmgb1 | 0.000703942 | -0.38 |
| ENSMUST00000148973 | Capns1 | 0.004092204 | -0.54 |
| ENSMUST00000144414 | Klra13-ps | 0.00486799 | -0.64 |
| ENSMUST00000196446 | Ube2d3 | 0.007141274 | -0.75 |
| ENSMUST00000174001 | Ube2i | 0.010161674 | -5.37 |
| ENSMUST00000015800 | Hspa8 | 0.015001839 | -5.71 |
| ENSMUST00000041388 | Serpine1 | 0.018200738 | 1.10 |
| ENSMUST00000184437 | Mir6236 | 0.024340342 | -0.53 |
| ENSMUST00000023072 | Parvb | 0.027014186 | 0.89 |
| ENSMUST00000178228 | C2cd4c | 0.034141132 | 1.04 |
| ENSMUST00000134214 | Gm49450 | 0.041472155 | -0.28 |
| ENSMUST00000025931 | Pdcd4 | 0.041472155 | -0.26 |
| ENSMUST00000125827 | Dtx2 | 0.041472155 | -4.71 |
| ENSMUST00000176216 | Cux1 | 0.041472155 | -5.50 |
| ENSMUST00000091269 | Erbin | 0.048618383 | -0.32 |

# Fig. 7

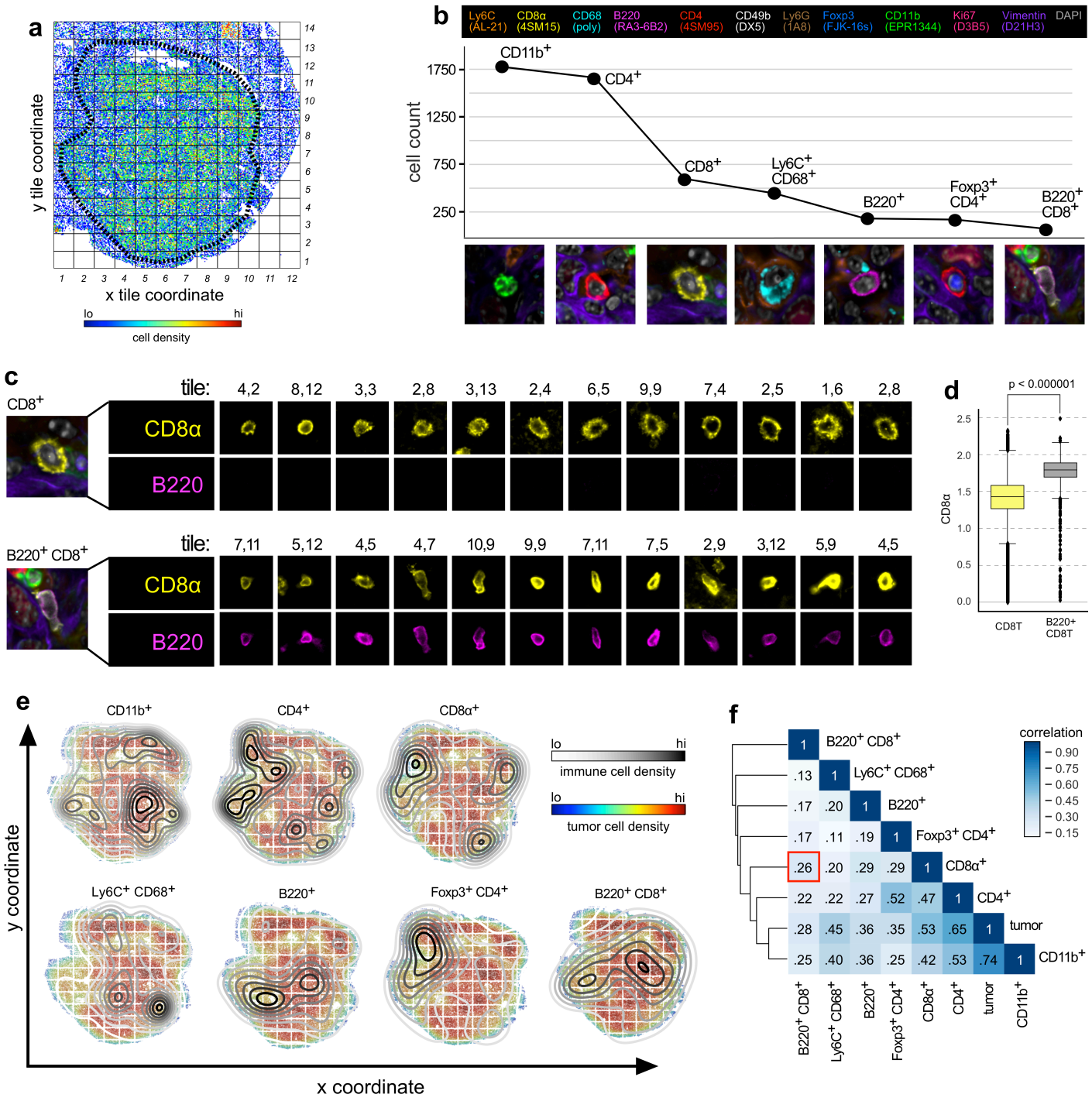
a
y tile coordinate
x tile coordinate
lo
hi
cell density
b
Ly6C (AL-21)
CD8α (4SM15)
CD68 (poly)
B220 (RA3-6B2)
CD4 (4SM95)
CD49b (DX5)
Ly6G (1A8)
Foxp3 (FJK-16s)
CD11b (EPR1344)
Ki67 (D3B5)
Vimentin (D21H3)
DAPI
cell count
CD11b+
CD4+
CD8+
Ly6C+ CD68+
B220+
Foxp3+ CD4+
B220+ CD8+
c
CD8+
tile: 4,2 8,12 3,3 2,8 3,13 2,4 6,5 9,9 7,4 2,5 1,6 2,8
CD8α
B220
B220+ CD8+
tile: 7,11 5,12 4,5 4,7 10,9 9,9 7,11 7,5 2,9 3,12 5,9 4,5
CD8α
B220
d
p < 0.000001
CD8α
CD8T
B220+ CD8T
e
CD11b+
CD4+
CD8α+
Ly6C+ CD68+
B220+
Foxp3+ CD4+
B220+ CD8+
lo
hi
immune cell density
tumor cell density
y coordinate
x coordinate
f
correlation
B220+ CD8+
Ly6C+ CD68+
B220+
Foxp3+ CD4+
CD8α+
CD4+
tumor
CD11b+

# Fig. 8

normal human WBCs

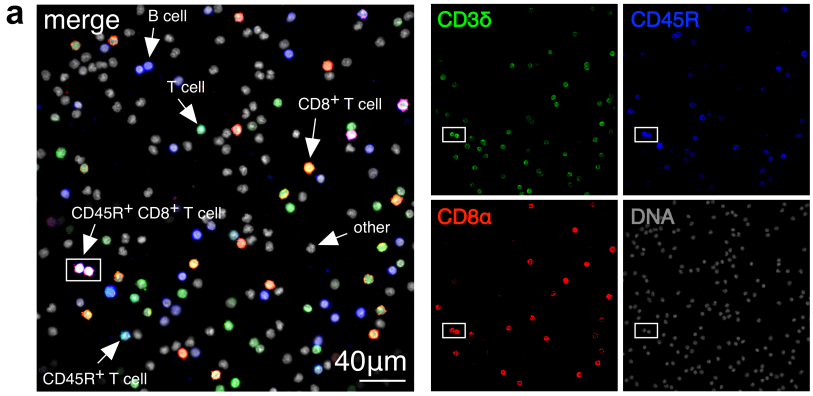


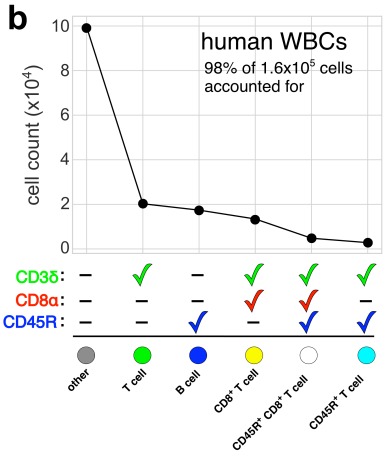

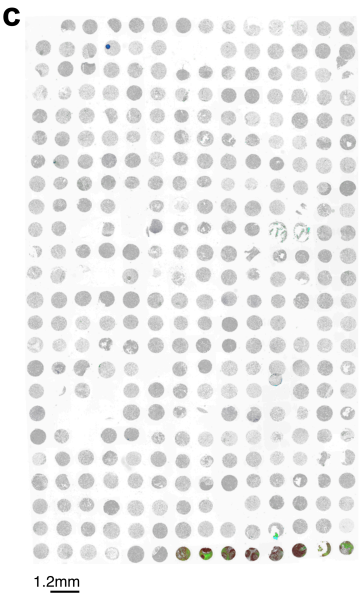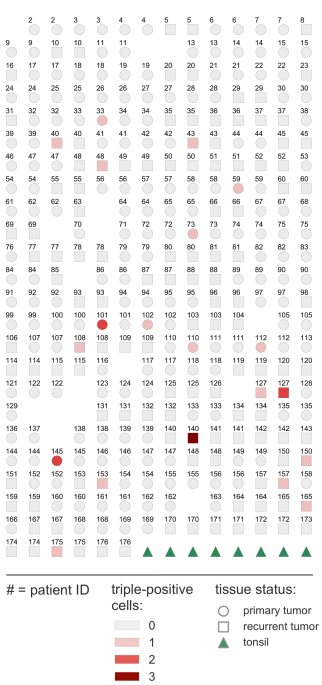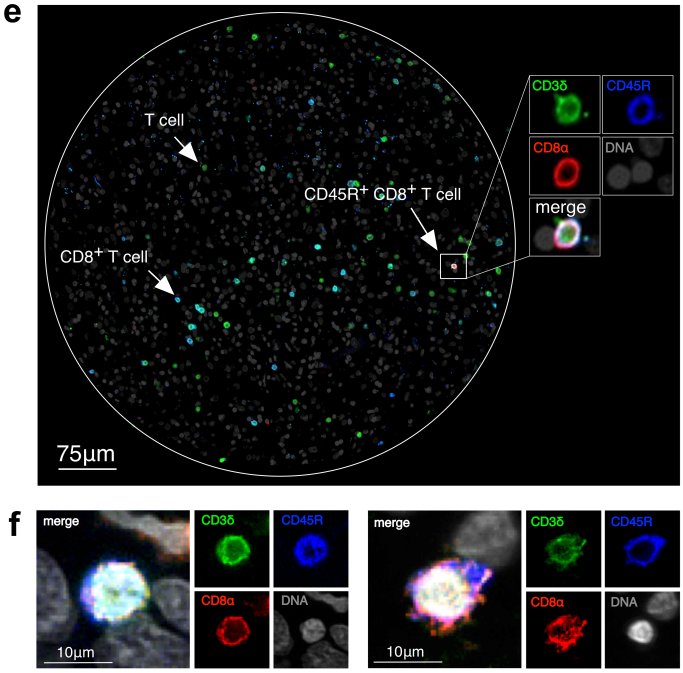
human brain tumor biopsies